The Illumination of Thunderclouds by Lightning:

Part 4: Volumetric Thunderstorm Imagery

Michael Peterson[1], Douglas Mach[2]

[1] ISR-2, Los Alamos National Laboratory, Los Alamos, New Mexico

[2]Science and Technology Institute, Universities Space Research Association, Huntsville, AL, USA

Corresponding author: Michael Peterson (mpeterson@lanl.gov), B241, P.O. Box 1663 Los Alamos, NM, 87545

Key Points:

- Retrieving source altitude from each GLM flash at the group level makes it possible to generate thunderstorm imagery as volumetric grids
- Example 3D imagery is generated for a Colombia thunderstorm – including Flash Extent Density, Min Flash Area, and optical energy grids
- These 3D grids provide additional information about storm structure that are masked by the vertical integration in the current 2D grids

LA-UR-21-25408

Abstract

Optical instruments such as the Geostationary Lightning Mapper (GLM) detect lightning based on transient changes in cloud illumination. The horizontal location of lightning is determined from the coordinates of the pixels on the imaging array illuminated during the flash. However, the vertical position of the lightning pulses (approximated by GLM "groups") below the cloud-top cannot be routinely determined from a single space-based instrument. In our prior work, we have developed a machine learning algorithm that can infer optical source altitude for a given pulse based on how the optical energy is distributed across the group footprint. In this fourth part of our thundercloud illumination study, we leverage these source altitudes to generate volumetric GLM imagery of a Colombia thunderstorm. We find that 3D versions of the current GLM meteorological imagery products (that describe thunderstorm kinematics) and thundercloud imagery products (that depict how the flash appears from space) provide additional insights into lightning activity in the thunderstorm are lost in the vertical integration used to generate the current 2D GLM gridded products. This new volumetric imaging capability provides a more comprehensive picture of where lightning occurs in the storm, how its physical characteristics vary across three-dimensional space, and how its optical emissions interact with surrounding the cloud medium.

Plain Language Summary

Optical lightning imagers including NOAA's Geostationary Lightning Mapper (GLM) detect lightning by recording the Earth from space with a specialized high-speed camera that triggers whenever one of its pixels brightens in response to lightning illuminating the surrounding clouds. Lightning can be located and have its structure mapped in two-dimensions by recording which pixels light up during the flash and projecting their angular coordinates down to the Earth. GLM data and imagery products are generated from this 2D composite view of the lightning activity in the thunderstorm. However, this is not a complete picture, as the frequency and behavior of lightning differs between vertical levels. We previously developed a method for retrieving source altitude based on how the energy from the optical pulses are spread horizontally across the cloud. In this study, we use these altitude estimates to construct 3D GLM imagery products that describe lightning across the full volume of the parent thunderstorm. This volumetric imagery provides additional insights into lightning and thunderstorms that are lost in the vertical integration employed by the current 2D GLM imagery products.

1 Introduction

In Peterson et al. (2021c), we demonstrated that it is possible to retrieve the source altitude for individual optical pulses (termed "groups") detected by a lightning imager – particularly NOAA's Geostationary Lightning Mapper (GLM: Goodman et al., 2013; Rudlosky et al., 2019) – from measurements of the spatial energy distribution provided by the instrument. Groups generated by high-altitude sources take on a substantially different appearance than groups from low-altitude sources (Peterson, 2020) because increased scattering over a thicker cloud layer broadens the spatial and temporal energy distributions (Light et al., 2001a,b; Koshak et al., 1994; Suszcynsky et al., 2000). As a result, low-altitude groups have broad and textured spatial distributions of radiant energy, while high-altitude groups might have almost all their optical energy concentrated in a single pixel – as shown previously with GLM groups coincident with Gigantic Jets that leave the cloud-top (Boggs et al., 2019). In previous work (Peterson et al., 2021c), we examined flashes in a thunderstorm with altitudes provided by a Lightning Mapping Array (LMA: Rison et al., 1999) in central Colombia. We then used machine learning methods to find which combination of group metrics describing the amplitude, breadth, and texture of the group spatial energy distributions provided the best balance between altitude prediction accuracy and computational expense. The resulting random forest model was able to not only reproduce the GLM-matched LMA altitude distributions throughout the time history of the thunderstorm with a median absolute error of 1.33 km, but also correctly map the vertical development of individual flashes (Peterson et al., 2021c).

While adding altitude information to Level-2 GLM cluster feature data will be useful for GLM analyses of lightning physics, its primary benefit is expected to be in the generation of

gridded products. GLM-derived meteorological imagery (Bruning et al., 2019) is the preferred data product for forecasters, and it is currently produced as a collection of two-dimensional grids that aggregate flashes from all vertical levels in the storm. Gridded products can be divided into four general categories: lightning rate girds – including Flash Extent Density (FED: Lojou and Cummins, 2004) and Group Extent Density (GED); flash characteristic grids – including Average Flash Area (AFA), Mean Flash Extent (MFEx), and Minimum Flash Area (MFA); cloud illumination grids – including Total Optical Energy (TOE) and the measured / modeled energies in Peterson (2019a); and thunderstorm retrieval grids – including the cloud type product in Peterson et al. (2020a). Note that while NOAA only routinely produces a subset of the GLM grids that have been developed by the lightning community (and the list above is also not comprehensive), any of the gridded products may be constructed from the Level-2 GLM cluster feature data using the glmtools Python package (Bruning et al., 2019) or other event-based or group-based gridding techniques.

The lack of altitude information is a key limitation for the current two-dimensional gridded products because lightning imagers including GLM preferentially detect flashes close to the cloud top (Thomas et al., 2000) and these high-altitude flashes have different characteristics than low-altitude flashes. Frequent small flashes above 10 km altitude have the same impact on FED, AFA or TOE values as the infrequent large flashes that originate near the cloud base. Thus, trends in these gridded products result not only from changes in flash rates and flash structure in response to thunderstorm kinematics, but also from changes in the flash altitude distribution. A key example of this is how AFA tends to increase outward from the storm core. While this can result from anvil or stratiform flashes increasing flash sizes outside of the convective core following the natural opposition between flash rate and flash area (Bruning and MacGorman,

2013), the more common cause of this behavior is energetic low-altitude sources illuminating surrounding cloud regions that do not produce lightning and are not otherwise illuminated by dimmer flashes (Peterson et al., 2017).

Using GLM retrieved altitudes to construct volumetric grids for these products will allow us to compare the behavior of lightning at different vertical layers within a given thunderstorm. This fourth part of our thundercloud illumination study uses the GLM-retrieved altitudes from the Colombia thunderstorm in Peterson et al. (2021c) to demonstrate the utility of these new volumetric GLM gridded products in documenting lightning behavior and measuring thundercloud illumination from each vertical level.

2 Data and Methodology

The Colombia thunderstorm case that we have been examining since Part 1 (Peterson et al, 2021a) occurred on 01 November 2019 in the vicinity of the Colombia LMA (COLLMA: Lopez et al., 2016; Aranguren et al., 2018). The thunderstorm and its lightning activity are described in detail in Peterson et al. (2021a). The storm is an interesting case for GLM because (1) it occurred near the satellite subpoint where parallax is small and instrument thresholds are low, making it possible to resolve flashes accurately and with an exceptional level of detail, and (2) it contained a diverse collection of lightning (including long horizontal stratiform flashes) over a large vertical depth extending beyond 15 km altitude due to high tropopause heights in the inner tropics.

Section 2.1 will describe GLM measurements of this Colombia thunderstorm case. Section 2.2 will briefly discuss the machine learning model developed in Peterson et al. (2021c)

for retrieving source altitudes for arbitrary GLM groups. Finally, Section 2.3 will address how volumetric grids are generated from the GLM data.

2.1 GLM Cluster Feature Data

GLM is a lightning imager that is based on the design of NASA's Optical Transient Detector (OTD: Christian et al., 2003) and Lightning Imaging Sensor (LIS: Christian et al., 2000; Blakeslee et al., 2020). These optical instruments record the cloud-top brightness of the scene below the satellite in a narrow spectral band around the 777.4 nm Oxygen emission line triplet at a high frame rate (nominally 500 FPS). An "event" is generated whenever the radiant energy in one of its pixels during a single 2-ms frame exceeds a specified threshold above the slowly changing background illumination at that pixel. These events are the basic building-blocks of lightning detections and describe portions of the cloud-top that are momentarily illuminated during a lightning process. Individual events do not describe complete lightning pulses. Optical sources may be larger than a GLM pixel or occur at pixel corners (Zhang et al., 2020) in some cases. However, even the abundant smaller lightning sources illuminate cloud areas much larger than a pixel via scattering through the cloud medium if they are sufficiently bright (Suszcynsky et al., 2001).

Lightning imagers employ clustering algorithms to translate event data into features that describe distinct lightning processes. Beginning with the LIS/OTD missions, features have been defined to approximate individual optical pulses (termed "groups") and complete lightning flashes (Mach et al., 2007; Mach, 2020). Groups are defined as clusters of events that fill a contiguous region on the instrument's imaging array. Flashes are defined as clusters of groups

that occur in close spatial and temporal proximity based on either a box-distance model (OTD) or a Weighted Euclidian Distance (WED) model (LIS, GLM).

GLM clustering is performed in real time by the lightning Cluster Filter Algorithm (LCFA: Goodman et al., 2010). This algorithm is based on the LIS clustering algorithm, but its group-to-flash clustering uses the OTD distance threshold to account for the larger GLM pixels and proximity is determined from the constituent event data for each group rather than the group centroids. In addition to these changes to the clustering algorithm from LIS to GLM, the strict GLM latency requirements have led to hard thresholds being coded into the LCFA that terminate flashes once they reach a certain level of complexity. These thresholds of 101 events per group, 101 groups per flash, and a 3 s flash duration are not based on lightning physics and are far stricter than the previous LIS thresholds of 2000 groups per flash and 30 s in flash duration (Peterson et al., 2017). When a flash is terminated for violating one of these thresholds, it will be marked with a "degraded" quality flag in the operational GLM data and any subsequent events / groups will define a new and independent flash feature. This causes cases of long horizontal lightning megaflashes (Lyons et al., 2020; Peterson et al., 2020b; Peterson, 2021a) to be split into multiple (often tens of) "flash" features in the GLM LCFA data with all but the final emissions along each branch being designated as degraded quality.

Subsequent data products – including the meteorological imagery described in Bruning et al. (2019) – assume that the LCFA clusters the event data correctly up to the flash level. However, these long-horizontal megaflashes that are artificially split by the LCFA are prominent outside of the convective core and are largely responsible for the spatial variations in the flash characteristic grids that reveal thunderstorm organization and structure. Grids like AFA and MFA differentiate between small convective flashes and large stratiform flashes. However, if the

large stratiform flashes are split into 101-group pieces with smaller areas than the overall flash, the contrast between convective and stratiform lightning will be reduced by even up to 1-2 orders of magnitude, as in the case of the 114,000 km^2 GLM flash discussed in Peterson (2019b).

Fortunately, the events and groups that comprise these split flashes are preserved in the operational GLM data and can be repaired to encapsulate the complete and distinct lightning flashes intended by the clustering algorithm in the LCFA. Peterson (2019b) developed software to repair the GLM flash cluster data, which has since been improved to handle cases of flashes split between separate data files. This software also adds flash metrics that better describe the development of each flash than the standard parameters in the operational LCFA data and adds a feature level between groups and flashes to represent lightning activity between their 2 ms and 330 ms time scales. These "series" features (Peterson and Rudlosky, 2019) capture periods of sustained optical emission from the flash and approximate sub-flash processes such as K-waves (Winn et al., 2011) and continuing current (Bitzer, 2017).

We will use this reprocessed GLM dataset (known as GLM-CIERRA: Peterson, 2021b) to construct the volumetric gridded products, as it provides a scientifically-accurate picture of GLM flashes at all scales – including new world records for flash distance (709 km) and duration (16.73 s) that have recently been recognized by the World Meteorological Organization (WMO) (Peterson et al., 2020b).

2.2 Retrieving Source Altitudes for GLM Groups

In Peterson et al. (2021c), we used Python's scikit-learn module (Pedregosa et al., 2011) to construct a random forest machine learning model for predicting the average altitude of COLLMA sources matched with GLM groups from group-level metrics describing the spatial

198 distribution of optical energy across the group footprint. COLLMA data were provided over a
199 1.7º longitude (74.5º W – 72.8º W) by 1º degree latitude (6.5 º N – 7.5º N) box within the LMA
200 domain by Lopez (2020, personal communication) and LMA sources within a 10-km/10-ms
201 window around a group footprint were assigned as "events" to the group of interest. If RF
202 sources could match multiple groups in a series, the brightest matching group was chosen for
203 assignment. The average matched source altitude was assumed to correspond to the altitude of
204 the lightning channel that generated the optical emissions responsible for the group. However,
205 since LMA sources are defined from a bottom-up view of the storm and GLM measurements of
206 thundercloud illumination depend on the thickness of the cloud layer between the source and the
207 cloud top, we use LMA altitudes that have been normalized relative to the local Advanced
208 Baseline Imager (ABI: Schmit et al., 2017) Cloud Top Height (CTH) product (Heidinger, 2011),
209 rather than the absolute LMA altitudes.

210 The input feature data is comprised of a subset of 16 metrics (Table 1 in Peterson et al.,
211 2021c) that describe the amplitude, breadth, and texture of the spatial energy distributions for
212 GLM groups, the local estimated GLM threshold that the flash was subject to, and the spatial
213 extent of the process (series) that produced the group. A detailed description of the parameter
214 selection and model training process is provided in Peterson et al. (2021c). The resulting random
215 forest model had an overall median absolute error for multi-event groups of 1.33 km in the
216 testing dataset. We applied the model to the full Colombia GLM dataset for the 01 November
217 2019 storm and found that the GLM-retrieved altitudes resolved changes in the LMA-matched
218 vertical altitude distribution over the duration of the thunderstorm – including responses to
219 convective invigoration and maturation – and was able to map the three-dimensional
220 development of individual flashes Peterson et al. (2021c).

2.3 Constructing Volumetric GLM Gridded Products

To facilitate comparisons with the grids generated by NOAA, we base the X and Y coordinate systems of our grids on the GLM event pixels and add a Z dimension consisting of 1-km layers from 0 to 20 km. Gridded products are computed on this 3D grid based on the horizontal positions of their constituent events and the altitude retrieved for the group. The GED product, for example, loops through each event in the group and increments each voxel corresponding to the point (event longitude, event latitude, group altitude) by one. FED, meanwhile, sets all these voxels equal to one for a given flash and then computes the total for all flashes. The energy products are computed in the same manner but increment the 3D voxels by their local energy. Finally, the flash characteristic grids and thunderstorm retrieval grids compute the minimum / mean / maximum attributes of the flashes that extend into each voxel.

The construction of volumetric imagery is exemplified in Figure 1 for two different flashes: a convective flash (Figure 1a) and a long horizontal flash (Figure 1b). Note that the horizontal extent of the images are scaled to fill the plot, causing the long horizontal flash to appear to be closer in size to the convective flash than it is. The greyscale points represent the 3D positions of the GLM group centroids and are also projected onto the rear panels to show their longitude-altitude and latitude-altitude distributions. The groups are colored by time with darker shades representing groups near the beginning of the flash and lighter shades representing newer groups.

To compute the volumetric Group Extent Density, we find the voxels that correspond to each group and increment them by one. We can then visualize the 3D volume occupied by the groups in the flash (red boxes) or make contour plots representing horizontal / vertical slices

243 through the 3D grid. In this example, we integrate GED vertically through the domain in the
244 color contour below the plot to produce similar imagery to NOAA's 2D GED product, and
245 horizontally to generate longitude-altitude and latitude-altitude contour plots along the back of
246 the figure.

247 We can see from this imagery that both flashes begin (dark grey) at high altitudes in the
248 cloud and descended over time (lighter grey). The flash in Figure 1a also produced events
249 (boxes) that occurred far from the group centroids (greyscale points), indicating that the flash
250 was bright enough to illuminate distant cloud regions (particularly between 10 km and 13 km
251 altitude in this case). This poses a caveat for our methodology: we are assuming that all
252 illumination across these larger groups occurs at the same altitude. This may not be true near the
253 edge of the storm where the cloud depth can vary substantially across the group footprint, and we
254 can have cases of reflections off other nearby clouds. This does not appear to be an issue with the
255 long horizontal stratiform flash in Figure 1b, whose bright groups better reflect the group-level
256 structure of the flash.

257 All our storm-level volumetric imagery is generated by aggregating the GLM data over
258 all flashes during 15-minute GLM-CIERRA (Peterson, 2021b) data files aligned to the UTC
259 hour. In total, we generate 12 volumetric gridded products, which are listed in Table 1. While not
260 all products will be discussed for brevity, example imagery for each product will be included as
261 Supporting Information (SI).

262

263 **3 Results**

Our analysis of the volumetric GLM grids for the Colombia thunderstorm starts with a general discussion of time-altitude trends in the gridded products over the duration of the thunderstorm in Section 3.1. Then, we will examine snapshots from various points in the storm that illustrate the origins of these trends and demonstrate the value of having vertical information available when interpreting GLM imagery. This analysis will be divided into two parts: Section 3.2 will discuss the meteorological imagery (encompassing the lightning rates and flash characteristics categories from before), while Section 3.3 will discuss the thundercloud imagery grids (encompassing the GLM energy products) that approximate what a high-altitude aircraft or space-based sensor would capture on film while recording the storm from above (i.e., Figure 1 in Peterson, 2019a).

3.1 Time-Altitude Trends in GLM Gridded Products

As we discussed in Part 2 (Peterson et al, 2021b), trending gridded products over time can be problematic if the instrument threshold changes substantially over the analysis period. In the Colombia thunderstorm case, however, the approximate threshold remained below 1 fJ over most of the storm duration (see Figure 2 in Peterson et al, 2021b). Dramatic increases in threshold were only noted before 02:30 UTC when lightning activity was first entering the LMA data domain and after 12:30 UTC as the storm was dissipating – and these increases were only up to a maximum of 2 fJ. Thus, threshold changes are not expected to be a significant source of bias in this case.

Time-altitude grids are shown in Figure 2 for FED, AFA, MFA, and MFEx and Figure 3 for TOE, Mean Flash Energy (MFEn), Mean Group Energy (MGE), and Mean Groups per Flash (MGPF). The white lines in each panel signify the maximum ABI CTH coincident with GLM

groups. Note that these timeseries are generated using only flashes that are matched to LMA sources, and flashes that occur outside of the LMA data domain (or that straddle its edges) are not considered here. We also provide the same plots constructed from the measured LMA source altitudes for each group rather than the GLM predictions as Supporting Information in Figure S1 and Figure S2 to show that variations in the time-altitude distributions for these gridded products are independent of the method used to resolve altitude.

Two distinct periods of lightning activity on 01 November 2019 can be noted in Figures 2 and 3: a short earlier period around 03:00 UTC where thunderstorm activity grazed the southern boundary of the LMA data domain (Figure 1f in Peterson et al, 2021a), and a longer period from 05:30 UTC until 13:00 UTC that contained most of the lightning activity mapped by both GLM and the LMA. This later period included three episodes of convective invigoration (around 07:00 UTC, 09:00 UTC, and 10:00 UTC) where peaks in the GLM group rates and LMA source rates could be noted in Figure 2 of Peterson et al, 2021a. The volumetric FED plot in Figure 2a here not only has local maxima corresponding to the peaks in these periods, but also increases in flash activity specifically at high altitudes, reflecting the increase in cloud height in response to the strengthening updraft (particularly for the 08:00 UTC and 10:00 UTC peaks).

These periods of intensification are accompanied by a reduction in flash area over most of the vertical column in Figure 2b. The key exception to this is with flashes that are located near the cloud base, whose AFA values generally remain above 1500 km^2 throughout the storm duration. The MFA plot in Figure 2c amplifies this contrast between lightning at the cloud base and lightning higher in the thunderstorm. The large values come from both convective flashes that illuminate large areas of nearby clouds and long horizontal stratiform flashes. While these two types of large flashes can be difficult to separate in the standard grids produced by NOAA,

the Mean Flash Extent product (Figure 2d) captures long horizontal flashes while not being particularly sensitive to flashes that happen to illuminate a large area of nearby cloud. This product shows that most of the large-area flashes during the earlier periods (05:00 – 10:00 UTC) illuminated cloud regions far beyond the extent of their group-level structure, while the later large flashes were cases of long horizontal lightning.

The TOE grid in Figure 3a resembles the FED grid from Figure 2a but is more concentrated in the 10-12 km layer than FED and has an unmatched low-altitude peak in the 12:00 UTC hour. These differences result from variations in the amount of energy provided by each flash (Figure 3b) and group (Figure 3c) as well as the number of optical pulses that are resolved from each flash (Figure 3d) at each altitude. Before the storm begins to dissipate around 11:00 UTC, flashes in the vertical layers around the LMA source peak (~10 km altitude) consist of more groups than the flashes that are near either the cloud base or the cloud top (Figure 3d). The low-altitude groups can be more energetic than groups above 7 km altitude (Figure 3c), but the few bright groups that can be resolved from such low altitudes are not sufficient to overcome the total energy contributed by the frequent dim groups that are detected higher up. Thus, the Mean Flash Energy (Figure 3b) near the cloud base is not remarkable in this plot, and the TOE values from these lower layers are small compared to layers around the 10-km LMA peak.

The exception to this behavior is when the storm begins to dissipate and long horizontal stratiform flashes become prominent. Flash altitudes decrease and flash rates fall after the 10:00 UTC peak, while the gridded products begin to change to reflect the organization and structure of the dissipating storm. These changes are most prominent around 12:00 UTC where low-altitude peaks form in the AFA, MFA, and Mean Flash Extent grids in Figure 2. The larger flashes

331 responsible for these peaks have more groups per flash (Figure 3d) and produce more energy per
332 group (Figure 3c) or flash (Figure 3b), leading to the second-highest TOE peak in Figure 3a.

333 This behavior at low altitudes in the storm would not be as notable in the current 2D
334 gridded products because they integrate the lightning activity from all vertical levels. As GLM
335 has a detection advantage for sources closer to the cloud top, the 2D grids for this storm would
336 be biased towards the smaller flashes near the 10-km LMA source maximum. Constructing
337 volumetric grids allows us to resolve nuances in the meteorological and thundercloud imagery
338 that are not apparent in the standard 2D gridded products generated by NOAA.

339

340 *3.2 Meteorological Imagery from Volumetric GLM Grids*

341 The time-altitude grids in Section 2.1 provide an overview of lightning activity within the
342 LMA data domain that still might integrate the behavior of lightning in multiple distinct
343 thunderstorms. In this section, we will examine spatial variations in lightning rates and flash
344 characteristics between 09:30 UTC and 10:30 UTC, surrounding the third and strongest period of
345 intensification. To gain a broader perspective on the lightning activity in the region, we will no
346 longer exclusively consider GLM groups that are matched to LMA sources, or even groups that
347 occur within the LMA data domain. Instead, all GLM data from the Colombia thunderstorm will
348 be analyzed within 2 degrees latitude or longitude from the center of the LMA data domain.

349 ABI Channel 14 (11.2 μm) infrared brightness temperatures for the 09:00 UTC and 10:00
350 UTC hours are shown across central Colombia in Figure 4. The box outlined in the center of
351 each panel corresponds to the LMA data domain used in the analyses in Figure 1 and Figure 2.

This period describes the merger of two cold cloud features (contiguous regions of ABI CH4 IR $T_b < 215$ K). The larger feature in the southwest corner of Figure 4a depicts a large Mesoscale Convective System (MCS) with an expansive stratiform region extending to the southwest. This feature was first noted around 02:00 UTC and grew over the next four hours before encroaching upon the LMA data domain by 06:00 UTC. The second northern feature describes a convective cell that developed in isolation around 06:00 UTC and moved to the southwest towards the approaching MCS as it grew into a larger storm over the next three hours. As the features began to merge by 09:00 UTC (Figure 4a), warming could already be noted in the ABI CH14 IR T_b values within the southern feature, indicating that the feature was beginning to dissipate. Meanwhile, the newer northern feature still had cloud-top temperatures < 196 K. The merger of these features over the two-hour period shown in Figure 4 was accompanied by intensification, resulting in decreasing infrared brightness temperatures over a large fraction of the LMA data domain.

To examine how the lightning responded to these developments, Figures 5 to 11 summarize the 3D gridded products by plotting horizontal and vertical integrations through the domain mapped in Figure 4. Figure 5 shows GLM FED at 09:30 UTC – at the beginning of the period in Figure 2a where FED values began to rise throughout the column and specifically near the cloud-top. The top-down integration in Figure 5a is consistent with the current 2D grids (though, not downscaled to the finer ABI fixed grid), while the horizontal integrations in the panels next to the map show the latitude-altitude (Figure 5b) and longitude-altitude (Figure 5c) distributions of FED across the mapped region. As in Figure 4, the LMA data domain is indicated with a box in Figure 5a. Additionally, the maximum ABI CTH values coincident with GLM groups are indicated by solid line overlays in Figure 5b and Figure 5c.

The larger regions of ABI infrared brightness temperatures < 215 K contain multiple convective-scale features in the FED plots in Figure 5 that are aligned with the coldest cloud-tops in Figure 4. At 09:30 UTC, two such features can be noted: a northern FED maximum within the northern cold cloud feature that includes the overall FED maximum for the storm and extends down to 5 km altitude (Figure 5b), and a southern convective feature in the southern cold cloud feature that corresponds to the dissipating MCS. Later, a convective feature further north within the northern cold cloud feature will form, which will we refer to as the "northernmost" convective feature to distinguish it from the northern convective feature shown here. Moreover, we use the term "convective core" to colloquially describe the region surrounding both (or all) convective features where at least 3 flashes occurred in the 15-minute window shown (i.e., 1 flash every 5 minutes).

The convective core is surrounded by lower FED values (1-2 flashes in the 15 minute window). These boundary regions are primarily populated by flashes at lower altitudes between 5 km and 10 km. Figure 6 plots the 3D MFA grid to better explain what these boundary flashes represent. The small flashes around the FED maxima (mostly in the northern feature) and larger flashes along the western flank of the storm are typical for the MFA product, but – as mentioned previously - they could result from either bright optical pulses interacting with nearby clouds or long horizontal stratiform flashes. Gradients in the ABI infrared imagery in Figure 4 suggests that the large MFA values along the northwest flank of the storm could result from edge illumination (as CH14 IR T_bs are much warmer than the in nearby convective core), while we would expect to find long horizontal flashes in the stratiform region extending from the southwestern flank of the convective core.

One method to verify this interpretation of the GLM data is to examine additional aspects of flash behavior in these regions. The MFEx and the number of Mean Groups per Flash (MGPF) gridded products differentiate between single radiant groups illuminating a cloud region and propagating flashes extending through that cloud region. Both products are included as SI, but we will show GPF in Figure 7. The GPF values in Figure 7a along the northwestern flank of the storm are low, confirming that these regions are illuminated occasionally by specific groups during large flashes. The GPF values in the southwestern flank of the storm, meanwhile, are exceptionally high - indicating that the average flash in this region produced 20+ groups whose events extended into each of these pixels. The latitude-altitude distribution in Figure 7b shows that these large GPF values occur exclusively at low altitudes in the cloud (< 10 km) extending southward from the southern convective feature. By contrast, mean GPF values are small at low altitudes in the northern convective feature and the large flashes here (Figure 6a) result from interactions with the lower cloud deck (IR T_b > 250 K in Figure 4c) along the northwestern flank rather than local lightning activity.

Between 09:30 UTC and 10:00 UTC (Figure 4c-e), the original southern convective feature continued to weaken while a new cell developed along the northern boundary of the LMA data domain. The original northern cell also intensified around 10:00 UTC, leading to lower ABI infrared brightness temperatures corresponding to higher cloud-top heights. Figure 8 shows the volumetric FED grid at 10:00 UTC. The ABI CTH traces in Figure 8c and d are ~2 km higher than in Figure 5 with significant lightning activity (FED > 30 flashes over the 15-minute period) extending beyond 15 km altitude. The MFA plot in Figure 9 shows that this increase in convective lightning is accompanied by a substantial decrease in MFA at all vertical levels

within the storm core due to the presence of flashes that illuminate the equivalent area of just 1-3 GLM pixels.

This suggests that the increase in column-integrated FED in Figure 5a is driven by frequent small convective flashes at high levels in the storm in response to the strengthening updraft that likewise caused flash heights to increase between 09:30 UTC and 10:00 UTC. However, the 3D grids also illustrate that despite the single smallest flashes decreasing in area, the AFA at low altitudes did not drastically change, and there were still some cases of large flashes along the western flank of the storm in Figure 9a. This increase in high-altitude FED was also accompanied by a decrease in low-altitude FED, though lightning continued to be detected at low altitudes over this period. Thus, these changes in the vertical source altitude distribution describe an upward migration in flash activity rather than a cessation of lightning activity at low levels. This can also be noted in the FED timeseries in Figure 2 (for GLM altitudes) and Figure S1 (for LMA altitudes). While not as prominent as in Figures 8 and 9 due to integrating all lightning activity over the LMA data domain into a single profile, the upward shift in source altitude is evident in these timeseries and reaches its maximum vertical displacement in the 10:15 UTC bin.

The storm begins to dissipate after 10:15 UTC. By 10:30 UTC, all convective features within the storm had started to weaken. The FED values in Figure 10 are notably lower than in the previous plots, though the MFA values in Figure 11 remained small following the convective burst. MFEx in Figure 2d was beginning to increase and, within the next hour, AFA (Figure 2b) and MFA (Figure 2c) would follow suit as the vertical peak in Mean Groups per Flash (Figure 3d) fell below 10 km altitude - marking the transition from a convective flash dominance to prominent non-convective lightning activity.

3.3 Thundercloud Imagery from Volumetric GLM Grids

The GLM energy grids listed in Table 1 show what GLM flashes look like embedded in the clouds. TOE, MFEn, and MGE all represent what an observer in space would record with a camera - with TOE representing a typical long (15-min) exposure, MFEn approximating the average energy on flash time scales (< 1 s) and MGE reporting the average energy on group time scales (2 ms). This conceptual approximation is not perfect for the latter two quantities, as they are computed by taking the TOE grid and dividing by either FED or GED. Thus, their actual definitions are the average amount of energy in a given pixel or voxel provided by each flash or group that illuminated that pixel or voxel. This reduces their dependence on lightning frequency to highlight variations in thundercloud illumination across the scene.

Thundercloud imagery can be more difficult to interpret than the meteorological imagery in the previous section because the amount of energy that is measured from orbit depends not only on the frequency and characteristics of lightning, but also the optical properties of the surrounding clouds. Where the lightning is located relative to the cloud structure (particularly with respect to altitude and proximity to cloud edges) will affect how the illuminated clouds appear from space. Therefore, features will be evident in the thundercloud imagery that are not apparent in the metrological imagery. The unique perspective provided by these products can be useful for tracking thunderstorm development and explaining trends in the meteorological imagery.

A key example is the case of radiance anomalies around convective clouds. We previously inferred that bright groups illuminating neighboring cloud regions resulted in the large flashes along the northern flank of the convective core. However, with MGE and MME, we

can directly see that there is increased illumination in this region. Figure 12 shows MGE imagery for the Colombia thunderstorm at 09:30 UTC. A greyscale color palette is used in this product to emphasize contrasts in the imagery. The vertical integration in Figure 12a shows a considerable amount of texture across the scene surrounding the convective features from Figure 5a, including a low-energy region adjacent to the northern FED hotspot and two particularly bright regions located on the northern and southern flanks of the storm core. The volumetric imagery (Figure 12b and c) shows that these bright regions coincide with the large low-altitude flashes discussed in Figure 6 and Figure 7.

The northern MGE peak is part of a broader region of enhanced MGE that extends across the northwestern flank of the storm and wraps around to the western flank in Figure 12a. It also extends from 5 km altitude up 15 km altitude – thus, multiple pulses from all altitudes at the edge of the cloud are contributing to the northern MGE maximum in Figure 12a. In these cases, optical emissions from sources at the edge of the cloud can travel along a relatively clear path to the imager with reduced attenuation compared to transmitting through the full vertical cloud volume, and this leads to biases towards large / energetic flashes in the meteorological imagery. By comparison, the southern MGE maximum is part of a linear feature of enhanced MGE that extends southward from the dissipating MCS. This peak is located in a region where the bright MGE values are in a vertically thin layer that extends from 5 to 7 km altitude - far below the local cloud top. Optical emission depends on both the electrical current traversing the channel and the channel length. Flashes with long horizontal channels are thus able to generate more energy for a given current (particularly during strokes or K-changes) than small convective flashes, and this could result in the increased MGE values here.

The dark region near the northern FED maximum requires a more detailed analysis to explain. This four-pixel MGE feature extends throughout the vertical column, leading to the decreased MGE values south of the northern bright spot in Figure 12b. Our recent work with radiance anomalies offers two possibilities on how radiant events can be adjacent to some of the dimmest events: either there is a poorly transmissive cloud present, or there is no cloud at all to scatter photons towards the satellite. The low altitudes of these groups and cold ABI IR T_b values in Figure 4c rule out the latter explanation. Thus, it is likely a poorly-transmissive cloud that is preventing certain pixels from being illuminated in these GLM groups.

Figure 13 shows a representative large (>1000 km^2) group from this dark region. We perform the steps necessary to identify radiance anomalies (as in Peterson, 2020) and construct the Measured – Modeled Energy product from Table 1. This approach attempts to normalize the spatial energy measurements from individual GLM groups to compensate for the natural radiance fall-off with distance from the optical source, thus amplifying local contrasts in the radiance patterns from inhomogeneities in the cloud medium. The spatial energy distribution for the group is shown in Figure 13a. The group consisted of a single very bright event (356 fJ) and a footprint comprised of 96 other dimmer events that extended to the southwest, northwest, and northeast of the brightest event. Note that this footprint did not extend due south, and the GLM pixel adjacent to the 356 fJ event did not trigger. Instead, the footprint seems to wrap around the western edge of a feature in the cloud medium that is blocking the light in this particularly bright pulse from reaching orbit. This radiance anomaly was only a few events away from forming a hole in the group, as we saw previously with LIS, and other groups in the area (not shown for brevity) had similar difficulties penetrating this cloud region.

We plot the radial energy profile for this group in Figure 13b and then fit the data points to a 4-term Gaussian model to describe the radiance fall-off with distance from the brightest event in the group (dashed line). Unlike Peterson (2019), we now clamp the radiance profile to the origin at the brightest event and the most distant event radius by giving these points additional weight in the numerical model (equal to the total number of events in the group). We construct and record these Gaussian models for every GLM group that exceeds 1000 km^2 in illuminated area along with radiance metrics such as the Half Width of Half Maximum (dotted line in Figure 13b), but discard cases where the model fit is either unrealistic (constant or increasing energy with distance) or too far from the energies of the clamp points (> 5% in the normalized energy from Figure 13b).

As these issues are not a concern for the group in question, we can use its Gaussian model to compute an idealized spatial energy distribution in Figure 13c. Unlike the measured energy distribution in Figure 13a, there are no radiance anomalies present and GLM energy depends only on the radial distance from the brightest measured event. Note that there is no maximum distance or minimum energy in the modeled energy distribution. To mitigate bias from extrapolation below the local GLM threshold, we ignore all pixels that are either further from the origin than the most distant observed event or that are less energetic than the dimmest event in the group.

Finally, the measured energy distribution in Figure 13a is compared with the modeled energy distribution in Figure 13c to generate the imagery in Figure 13d. This energy comparison forms the basis for the thundercloud imagery in Peterson (2019) and the poorly transmissive cloud identification algorithm in Peterson (2020). However, we are presenting it here as a difference between measured and modeled energy in units of fJ rather than as a radiance ratio.

The Measured / Modeled Energy product gives each group an equal weight, regardless of its brightness, and highlights texture in the group spatial energy distribution at larger distances from the origin. The Measured – Modeled Energy shown in Figure 13d emphasizes contrasts near the origin and weights each group according to its maximum event energy. There are advantages to each approach, but we chose to introduce the energy difference product here because it reduces the impact of elongated optical sources (which produce higher-than-expected energies at large distances) while highlighting cases where optical emissions can escape the cloud along relatively-clear paths. For the group in question, this product clearly shows a measured energy deficit to the south and east of the brightest event in the group and a measured energy surplus in the northern and western regions where the group footprint wraps around the poorly transmissive cloud.

The Measured – Modeled Energy (MME) grids (i.e., Figure 13d) are accumulated from all GLM groups >1000 km^2 and the resulting volumetric MME imagery for 09:30 UTC is mapped in Figure 14 along with ABI CH14 infrared brightness temperatures (Figure 14a) as an overall vertical integration (Figure 14b) and at 6 different vertical levels. As before, the LMA data domain is indicated with a solid outline at the center of each panel. A prominent feature of this new imagery is that there is a pronounced low energy bias across the feature (cool colors). This results from when GLM does not record events at a certain pixel which the model suggests should have triggered due to its proximity to the brightest event. As in Figure 14d, this can occur as small differences along the edge of the group (< 1 fJ per group) or large differences near the brightest event in the group (on the order of 1-10 fJ per group). The first category of small differences can be problematic in high group rate environments because they are almost always negative and - despite individually meeting the 5% threshold mentioned above - their aggregate

554 sum introduces a non-trivial negative bias into the accumulated grids. To reduce this bias, we do
555 not allow contributions from the smallest energy differences in the sample. The minimum energy
556 difference that we consider 0.1 fJ in this case.

557 The panels in Figure 14 indicate regions where more energy than expected escapes the
558 cloud in red and regions that are darker than expected in blue. The vertical integration in Figure
559 14b masks the contributions from individual layers that are shown in the subsequent panels.
560 Many of the prominent features in Figure 14b originate below 9 km altitude (Figure 14d,e). The
561 high-altitude layers primarily describe distinct convective features that have an energy deficit at
562 their centers surrounded by an energy surplus where light can escape the side of the cloud. Two
563 of these features can be noted in Figure 14 (most visible in Figure 14f) that are aligned with the
564 older MCS feature in the south and the newer storm feature in the north from Figure 14a.
565 However, while the southern cold centers in each altitude layer are aligned vertically in Figure
566 14e-g, the northern cold feature has a southward tilt such that it is only aligned with the highest
567 cloud-tops from Figure 14a in the top layer that corresponds to 12-15 km (Figure 14g).

568 The reason for this apparent tilt is that the GLM MME grid is sensing the development of
569 the northernmost cold cloud feature between 09:30 UTC and 10:00 UTC. The cold centers in the
570 lower layers are displaced further north than the coldest ABI cloud tops because they describe
571 the illumination of this new feature while the higher cold centers are still sensing the older
572 northern feature that is aligned with the minimum ABI IR T_b. In the next ABI scan, the
573 northernmost convective feature would strengthen, generating a new FED maximum to the
574 northwest of the 09:30 UTC FED maximum (i.e., Figure 8a) with increasing ABI CTH values
575 and frequent lightning at high altitudes in the storm.

By the end of this period at 10:00 UTC, the MGE (Figure 15) and MME (Figure 16) features corresponding to the older MCS had largely eroded, leading to low MGE values mostly below 10 km altitude and only slight MME gradients. By contrast, the strengthening northern features each produced their own distinct vertically aligned MGE maximum and MME minimum that extended from the cloud-top down to at least 9 km altitude. The brightest pixels do not result from stratiform flashes or cases of edge illumination at this time step, but instead are collocated with the FED maxima. Unlike at 09:30 UTC, the highest MGE values come from the small and frequent high-altitude flashes that dominate the FED at this time and the increasing MGE with altitude results from the decreasing optical depth of cloud separating these flashes from the imager. Still, there are cases of groups with radiance anomalies that preferentially illuminate the gap between the two features rather than either feature. These groups have a nearly linear appearance and are responsible for the positive MME anomalies in Figure 16f and g.

While the location of the lightning sources relative to the cloud features is important for determining how the illuminated clouds appear from orbit, there is a general correlation between strengthening / weakening convection and the peak amplitude of the MME product. As with the northern convective feature, strong convection tends to have an energy deficit in the tens of femtojoules at individual vertical levels, while weakening convection might have an energy deficit around 1 fJ or smaller, or even a slight surplus. While the goal of this work is to demonstrate the 3D imaging capability, these results show that additional work is merited to examine how well these GLM thundercloud imagery products (including TOE, MFEn, and MGE) track changes in cloud products derived from radar, passive microwave, and infrared / visible thunderstorm measurements.

4 Conclusion

In this fourth part of our thundercloud illumination study, we use the GLM group-level source altitude retrieval developed in Peterson et al. (2021c) to construct volumetric meteorological and thundercloud imagery from the GLM data collected during a Colombia thunderstorm. Analyses of these 3D gridded products demonstrate that de-coupling the trends from lightning at different altitudes reveals aspects of thunderstorm development that are masked by the vertical integration in the current NOAA 2D GLM grids. Not only do flashes at low altitudes behave differently than lightning closer to the cloud top, but flash rates also vary with time and altitude.

Tracking these changes can be useful for diagnosing changes in convection (including invigoration and dissipation) that determine the risk of severe weather. Sudden increases or, "jumps", in the thunderstorm flash rate have been shown to be symptomatic of the convective invigoration that leads to severe weather events and Lightning Jump Algorithms (LJAs) have been developed for LMA data (Schultz et al., 2009) to predict imminent severe weather events. However, poor GLM detection of compact flashes at low altitudes (whose optical energy must transmit through a dense cloud medium to trigger GLM) poses a problem for identifying jumps in the flash rate data. GLM-derived flash altitudes could provide an alternate method for identifying these strengthening updrafts that is not adversely affected by poor GLM performance near the cloud base. Moreover, early periods of vertical development might be detected at low altitudes in the 3D meteorological or thundercloud imagery products (as we saw with MME in our discussion of Figure 16) before signals at high altitudes (i.e., the 2D FED and ABI products like CTH).

These 3D grids, if constructed for the full disk, would provide a more comprehensive picture of lightning activity across the GLM domain than the current 2D gridded products. Moreover, the 20 s update cycle of GLM data would enable rapid update volumetric imagery to be generated to complement imagery from the ABI mesoscale sectors. If this can be done in a time-efficient manner, then it would provide a tremendous value to the operational users of GLM data. However, the key challenge will be to develop a universal altitude retrieval that works for every storm type within the GLM FOV. Future work will improve the machine learning approach developed in Peterson et al. (2021c) for use with multiple types of thunderstorms across the GLM FOV and with the global data generated by LIS and OTD since 1995.

Acknowledgments

This work was supported by the US Department of Energy through the Los Alamos National Laboratory (LANL) Laboratory Directed Research and Development (LDRD) program under project number 20200529ECR. Los Alamos National Laboratory is operated by Triad National Security, LLC, for the National Nuclear Security Administration of U.S. Department of Energy (Contract No. 89233218CNA000001). The work by co-author Douglas Mach was supported by ASA 80MFSC17M0022 “Cooperative Agreement with Universities Space Research Association” and NASA Research Opportunities in Space and Earth Science grant NNX17AJ10G “U.S. and European Geostationary Lightning Sensor Cross-Validation Study.” We would like to thank the operators of the Colombia LMA at the Technical University of Catalonia and Dr. Jesús López for sharing their processed LMA data for the presented case. The data used in this study is available at Peterson (2021c).

References

Aranguren, D., Lopez, J., Montanya, J., & Torres, H. (2018, September). Natural observatories for lightning research in Colombia. In *2018 International Conference on Electromagnetics in Advanced Applications (ICEAA)* (pp. 279-283). IEEE

Bitzer, P. M. (2017). Global distribution and properties of continuing current in lightning. *Journal of Geophysical Research: Atmospheres*, *122*(2), 1033-1041

Blakeslee, R.J., Lang, T.J., Koshak, W.J., Buechler, D., Gatlin, P., Mach, D.M., Stano, G.T., Virts, K.S., Walker, T.D., Cecil, D.J., Ellett, W., Goodman, S.J., Harrison, S., Hawkins, D.L., Heumesser, M., Lin, H., Maskey, M., Schultz, C.J., Stewart, M., Bateman, M., Chanrion, O. and Christian, H. (2020), Three Years of the Lightning Imaging Sensor Onboard the International Space Station: Expanded Global Coverage and Enhanced Applications. *J. Geophys. Res. Atmos*., **125**: e2020JD032918. https://doi.org/10.1029/2020JD032918

Boggs, L. D., Liu, N., Peterson, M., Lazarus, S., Splitt, M., Lucena, F., ... & Rassoul, H. K. (2019). First observations of gigantic jets from geostationary orbit. *Geophysical Research Letters*, *46*(7), 3999-4006.

Bruning, E. C., & MacGorman, D. R. (2013). Theory and Observations of Controls on Lightning Flash Size Spectra, *Journal of the Atmospheric Sciences*, *70*(12), 4012-4029. https://doi.org/10.1175/JAS-D-12-0289.1.

Bruning, E., Tillier, C. E., Edgington, S. F., Rudlosky, S. D., Zajic, J., Gravelle, C., et al. (2019). Meteorological imagery for the geostationary lightning mapper. *Journal of Geophysical Research: Atmospheres*, 2019; 124: 14285– 14309. https://doi.org/10.1029/2019JD030874.

Christian, H. J., R. J. Blakeslee, S. J. Goodman, and D. M. Mach (Eds.) (200). Algorithm Theoretical Basis Document (ATBD) for the Lightning Imaging Sensor (LIS), NASA/Marshall Space Flight Center, Alabama. (Available as http://eospso.gsfc.nasa.gov/atbd/listables.html, posted 1 Feb. 2000).

Christian, H. J., Blakeslee, R. J., Boccippio, D. J., Boeck, W. L., Buechler, D. E., Driscoll, K. T., ... & Stewart, M. F. (2003). Global frequency and distribution of lightning as observed from space by the Optical Transient Detector. *Journal of Geophysical Research: Atmospheres*, *108*(D1), ACL-4.

Goodman, S. J., D. Mach, W. J. Koshak, and R. J. Blakeslee. (2010). *GLM Lightning Cluster-Filter Algorithm (LCFA) Algorithm Theoretical Basis Document (ATBD)*. Retrieved from https://www.goes-r.gov/products/ATBDs/baseline/Lightning_v2.0_no_color.pdf, posted 24 Sept. 2010

Goodman, S. J., R. J. Blakeslee, W. J. Koshak, D. Mach, J. Bailey, D. Buechler, L. Carey, C. Schultz, M. Bateman, E. McCaul Jr., and G. Stano, 2013: The GOES-R geostationary lightning mapper (GLM). *J. Atmos. Res.,* **125-126**, 34-49

Heidinger, A. (2011). Algorithm theoretical basis document ABI cloud height. *NOAA NESDIS Center for Satellite Applications and Research, http://www. goes-r. gov/products/ATBDs/baseline/Cloud_CldHeight_v2. 0 _no_color. pdf*.

Koshak, W. J., Solakiewicz, R. J., Phanord, D. D., and Blakeslee, R. J. (1994), Diffusion model for lightning radiative transfer, *J. Geophys. Res.*, 99(D7), 14361– 14371, https://doi.org/10.1029/94JD00022.

Light, T. E., Suszcynsky, D. M., and Jacobson, A. R. (2001a), Coincident radio frequency and

optical emissions from lightning, observed with the FORTE satellite, *J. Geophys. Res.*, 106(D22), 28223– 28231, https://doi.org/10.1029/2001JD000727.

Light, T. E., Suszcynsky, D. M., Kirkland, M. W., and Jacobson, A. R. (2001b), Simulations of lightning optical waveforms as seen through clouds by satellites, *J. Geophys. Res.*, 106(D15), 17103– 17114, https://doi.org/10.1029/2001JD900051.

Lojou, J.-Y., K. L. Cummins, 2004: On the representation of two- and three-dimensional total lightning information. In Preprints, Conference on Meteorological Applications of Lightning Data (pp. Paper 2.4, AMS Annual Meeting, San Diego, CA, USA)

López, J. A., Montanyà, J., van der Velde, O., Romero, D., Aranguren, D., Torres, H., ... & Martinez, J. (2016, September). First data of the Colombia lightning mapping array—COLMA. In *2016 33rd International Conference on Lightning Protection (ICLP)* (pp. 1-5). IEEE.

Lyons, W. A., Bruning, E. C., Warner, T. A., MacGorman, D. R., Edgington, S., Tillier, C., & Mlynarczyk, J. (2020). Megaflashes: Just how long can a lightning discharge get?. *Bulletin of the American Meteorological Society*, *101*(1), E73-E86.

Mach, D. M., Christian, H. J., Blakeslee, R. J., Boccippio, D. J., Goodman, S. J., & Boeck, W. L. (2007). Performance assessment of the optical transient detector and lightning imaging sensor. *Journal of Geophysical Research: Atmospheres*, *112*(D9).

Mach, D. M. (2020). Geostationary Lightning Mapper clustering algorithm stability. *Journal of Geophysical Research: Atmospheres*, *125*(5), e2019JD031900.

Pedregosa, F., Varoquaux, G., Gramfort, A., Michel, V., Thirion, B., Grisel, O., ... & Duchesnay, E. (2011). Scikit-learn: Machine learning in Python. *the Journal of machine Learning research*, *12*, 2825-2830.

Peterson, M. (2019a). Using lightning flashes to image thunderclouds. *Journal of Geophysical Research: Atmospheres*, 124, 10175– 10185. https://doi.org/10.1029/2019JD031055

Peterson, M. (2019b). Research applications for the Geostationary Lightning Mapper operational lightning flash data product. *Journal of Geophysical Research: Atmospheres*, 124, 10205– 10231. https://doi.org/10.1029/2019JD031054

Peterson, M. (2020). Modeling the transmission of optical lightning signals through complex 3-D cloud scenes. *Journal of Geophysical Research: Atmospheres*, 125, e2020JD033231. https://doi.org/10.1029/2020JD033231

Peterson, M. (2021a). Where Are the Most Extraordinary Lightning Megaflashes in the Americas?, *Bulletin of the American Meteorological Society*, *102*(3), E660-E671. Retrieved Apr 29, 2021, from https://journals.ametsoc.org/view/journals/bams/102/3/BAMS-D-20-0178.1.xml

Peterson, M. (2021b). GLM-CIERRA http://dx.doi.org/10.5067/GLM/CIERRA/DATA101

Peterson, M. (2021c). Coincident Optical and RF Lightning Detections from a Colombia Thunderstorm. https://doi.org/10.7910/DVN/5FR6JB, Harvard Dataverse, V1

Peterson, M., & Rudlosky, S. (2019). The time evolution of optical lightning flashes. *Journal of Geophysical Research: Atmospheres*, 124, 333– 349. https://doi.org/10.1029/2018JD028741

Peterson, M., Rudlosky, S., & Deierling, W. (2017). The evolution and structure of extreme optical lightning flashes. *Journal of Geophysical Research: Atmospheres*, 122, 13,370–13,386. https://doi.org/10.1002/2017JD026855

Peterson, M., Rudlosky, S., & Zhang, D. (2020a). Thunderstorm Cloud-Type Classification from Space-Based Lightning Imagers, *Monthly Weather Review*, *148*(5), 1891-1898. Retrieved

734 Apr 29, 2021, from https://journals.ametsoc.org/view/journals/mwre/148/5/mwr-d-19-
735 0365.1.xml
736 Peterson, M. J., Lang, T. J., Bruning, E. C., Albrecht, R., Blakeslee, R. J., Lyons, W. A., et al.
737 (2020b). New World Meteorological Organization certified megaflash lightning extremes
738 for flash distance (709 km) and duration (16.73 s) recorded from space. *Geophysical*
739 *Research Letters*, 47, e2020GL088888. https://doi.org/10.1029/2020GL088888
740 Peterson, M., Light, T., & Mach, D. (2021a). The Illumination of Thunderclouds by Lightning:
741 Part 1: The Extent and Altitude of Optical Lightning Sources. *Journal of Geophysical*
742 *Research: Atmospheres*.
743 Peterson, M., Light, T., & Mach, D. (2021b). The Illumination of Thunderclouds by Lightning:
744 Part 2: The Effect of GLM Instrument Threshold on Detection and Clustering. *Journal of*
745 *Geophysical Research: Atmospheres*.
746 Peterson, M., Light, T., & Mach, D. (2021c). The Illumination of Thunderclouds by Lightning:
747 Part 3: Retrieving Optical Source Altitude. *Journal of Geophysical Research:*
748 *Atmospheres*.
749 Rison, W., R. J. Thomas, P. R. Krehbiel, T. Hamlin, and J. Harlin, 1999: A GPS-based three-
750 dimensional lightning mapping system: Initial observations in central New Mexico.
751 *Geophys. Res. Lett.,* ***26***(23), 3573-3576. https://doi.org/10.1029/1999gl010856.
752 Rudlosky, S. D., Goodman, S. J., Virts, K. S., & Bruning, E. C. (2019). Initial geostationary
753 lightning mapper observations. *Geophysical Research Letters*, *46*(2), 1097-1104.
754 Schmit, T. J., Griffith, P., Gunshor, M. M., Daniels, J. M., Goodman, S. J., & Lebair, W. J.
755 (2017). A closer look at the ABI on the GOES-R series. *Bulletin of the American*
756 *Meteorological Society*, *98*(4), 681-698.
757 Schultz, C. J., Petersen, W. A., & Carey, L. D. (2009). Preliminary development and evaluation
758 of lightning jump algorithms for the real-time detection of severe weather. *Journal of*
759 *Applied Meteorology and Climatology*, *48*(12), 2543-2563.
760 Suszcynsky, D. M., Kirkland, M. W., Jacobson, A. R., Franz, R. C., Knox, S. O., Guillen, J. L.
761 L., and Green, J. L. (2000), FORTE observations of simultaneous VHF and optical
762 emissions from lightning: Basic phenomenology, *J. Geophys. Res.*, 105(D2), 2191–
763 2201, https://doi.org/10.1029/1999JD900993.
764 Suszcynsky, D. M., Light, T. E., Davis, S., Green, J. L., Guillen, J. L. L., and Myre, W. (2001),
765 Coordinated observations of optical lightning from space using the FORTE photodiode
766 detector and CCD imager, *J. Geophys. Res.*, 106(D16), 17897– 17906,
767 https://doi.org/10.1029/2001JD900199.
768 Thomas, R., P.R. Krehbiel, W. Rison, T. Hamlin, D. J. Boccippio, S. J. Goodman, and H. J.
769 Christian, 2000: Comparison of ground-based 3-dimensional lightning mapping
770 observations with satellite-based LIS observations in Oklahoma. *Geophys. Res. Lett.*, **27**,
771 12, 1,703-1,706.
772 Winn, W. P., Aulich, G. D., Hunyady, S. J., Eack, K. B., Edens, H. E., Krehbiel, P. R., Rison,
773 W., and Sonnenfeld, R. G. (2011), Lightning leader stepping, K changes, and other
774 observations near an intracloud flash, *J. Geophys. Res.*, 116, D23115,
775 doi:10.1029/2011JD015998.
776 Zhang, D., & Cummins, K. L. (2020). Time evolution of satellite-based optical properties in
777 lightning flashes, and its impact on GLM flash detection. *Journal of Geophysical*
778 *Research: Atmospheres*, *125*(6).
779

780 **Table 1.** List of GLM volumetric thunderstorm imagery products generated in this study.
781

Parameter Name	Units	Description
Flash Extent Density	#	Total flash count per voxel
Group Extent Density	#	Total group count per voxel
Mean Groups per Flash	#	Mean number of groups per flash in each voxel
Average Flash Area	km^2	Average illuminated area of all flashes in each voxel
Minimum Flash Area	km^2	Minimum illuminated area of all flashes in each voxel
Mean Flash Extent	km	Mean group-level extent of all flashes in each voxel
Mean Flash Duration	ms	Mean duration of all flashes in each voxel
Total Optical Energy	fJ	Total optical energy from all events in each voxel
Mean Flash Energy	fJ	Average optical energy in a given voxel from all flashes in that voxel
Mean Group Energy	fJ	Average optical energy in a given voxel from all groups in that voxel
Measured – Modeled Energy	fJ	Energy difference between GLM-measured TOE in a given voxel and the expected energy from modeling the radial energy distribution for each group

782

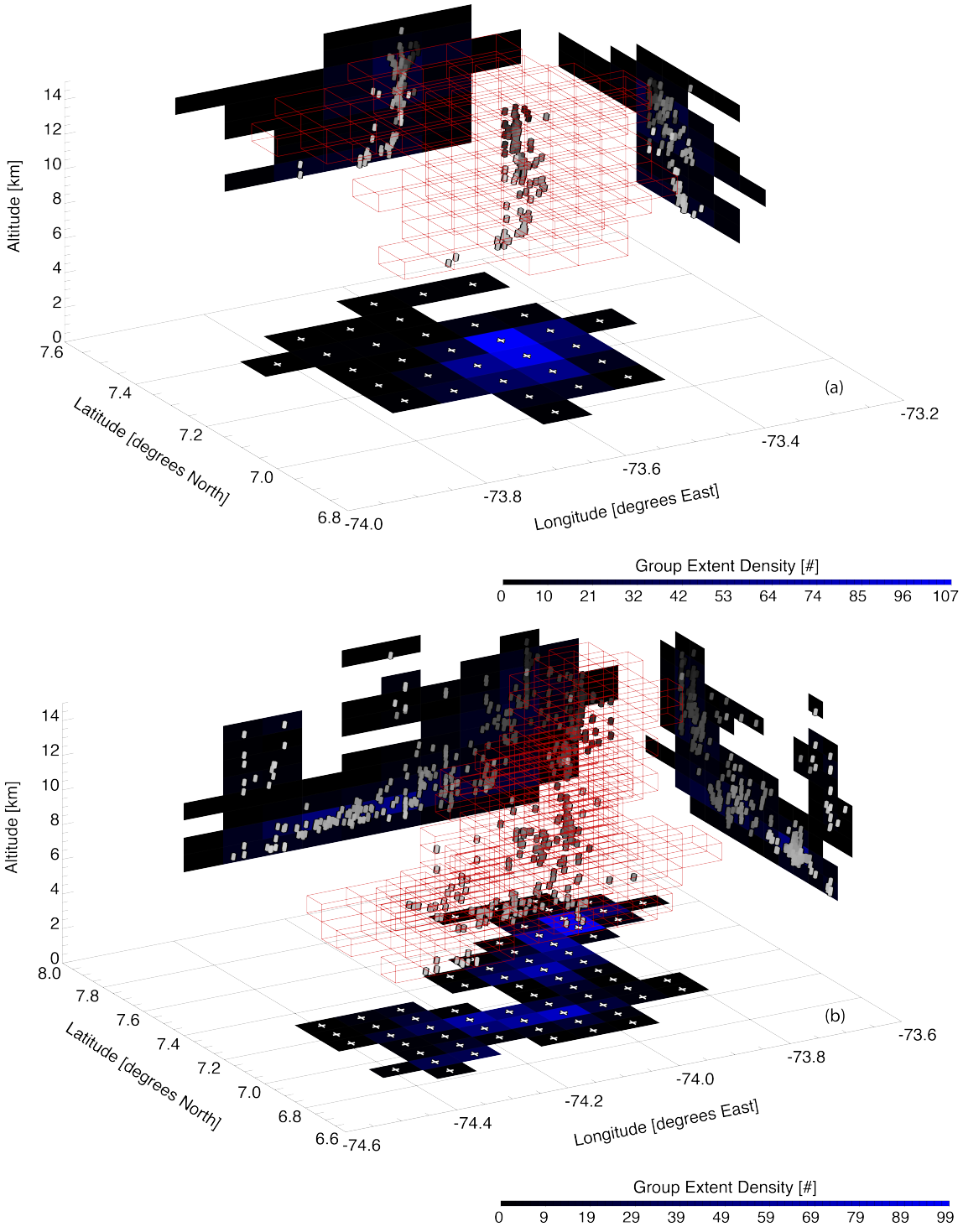

Figure 1. Volumetric GED for an example (a) primarily vertical flash and (b) long horizontal flash. Positions of GLM groups (greyscale by time order from dark to light) and voxels illuminated by their constituent events are shown in 3D space. Vertical projections of GED are mapped at z=0 km, while horizontal projections of GED and the group-level structure with longitude (back) and latitude (right) are plotted vertically. Note that each panel has a different latitude and longitude scale.

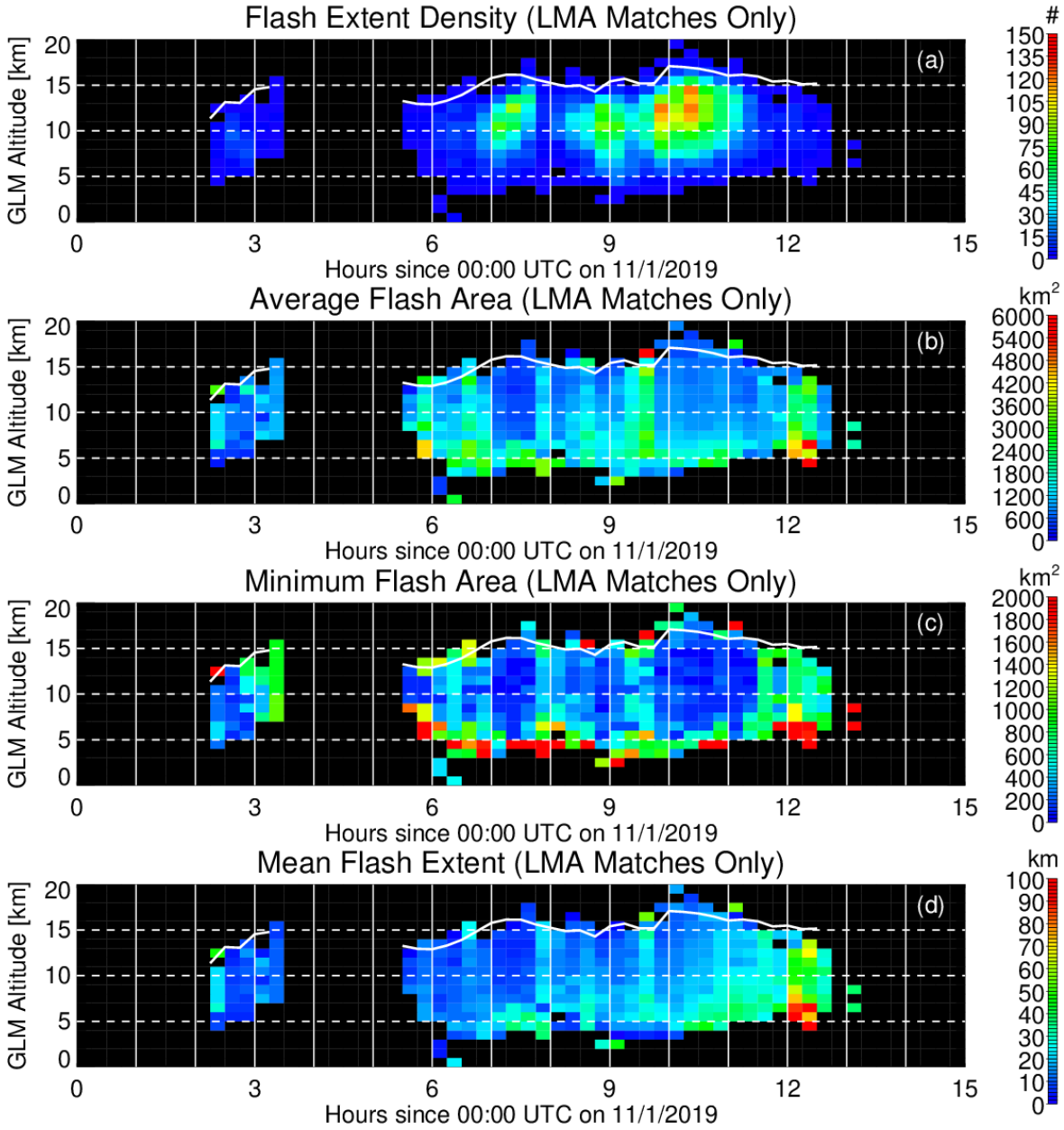

Figure 2. Timeseries of (a) FED, (b) AFA, (c) MFA, and (d) MFEx from LMA-matched GLM flashes in each 1-km altitude layer over the duration of the Colombia thunderstorm. The white lines in each panel signify the maximum ABI CTH coincident with the GLM groups.

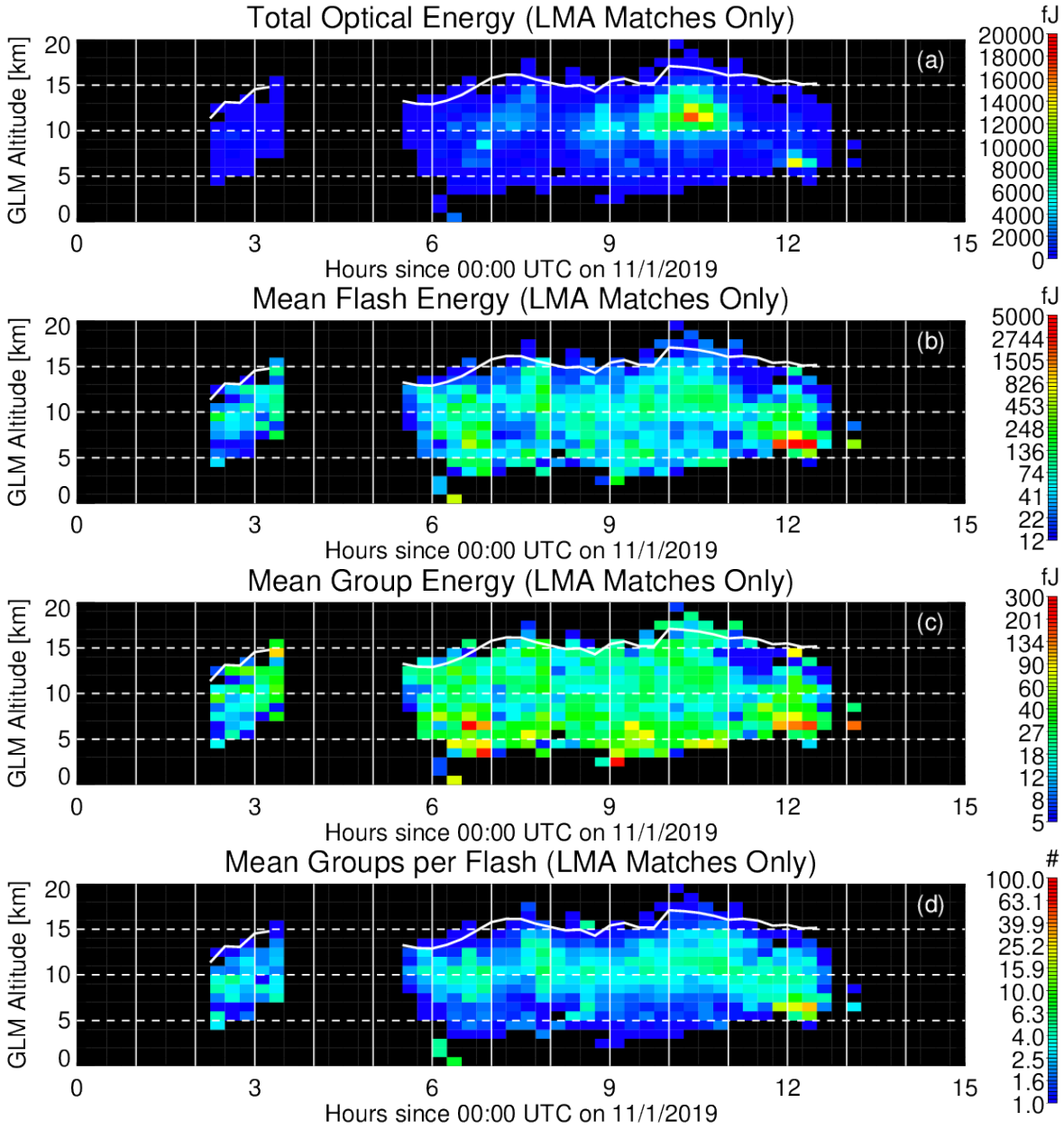

Figure 3. Timeseries of (a) TOE, (b) MFEn, (c) MGE, and (d) GPF from LMA-matched GLM flashes in each 1-km altitude layer over the duration of the Colombia thunderstorm. The white lines in each panel signify the maximum ABI CTH coincident with the GLM groups.

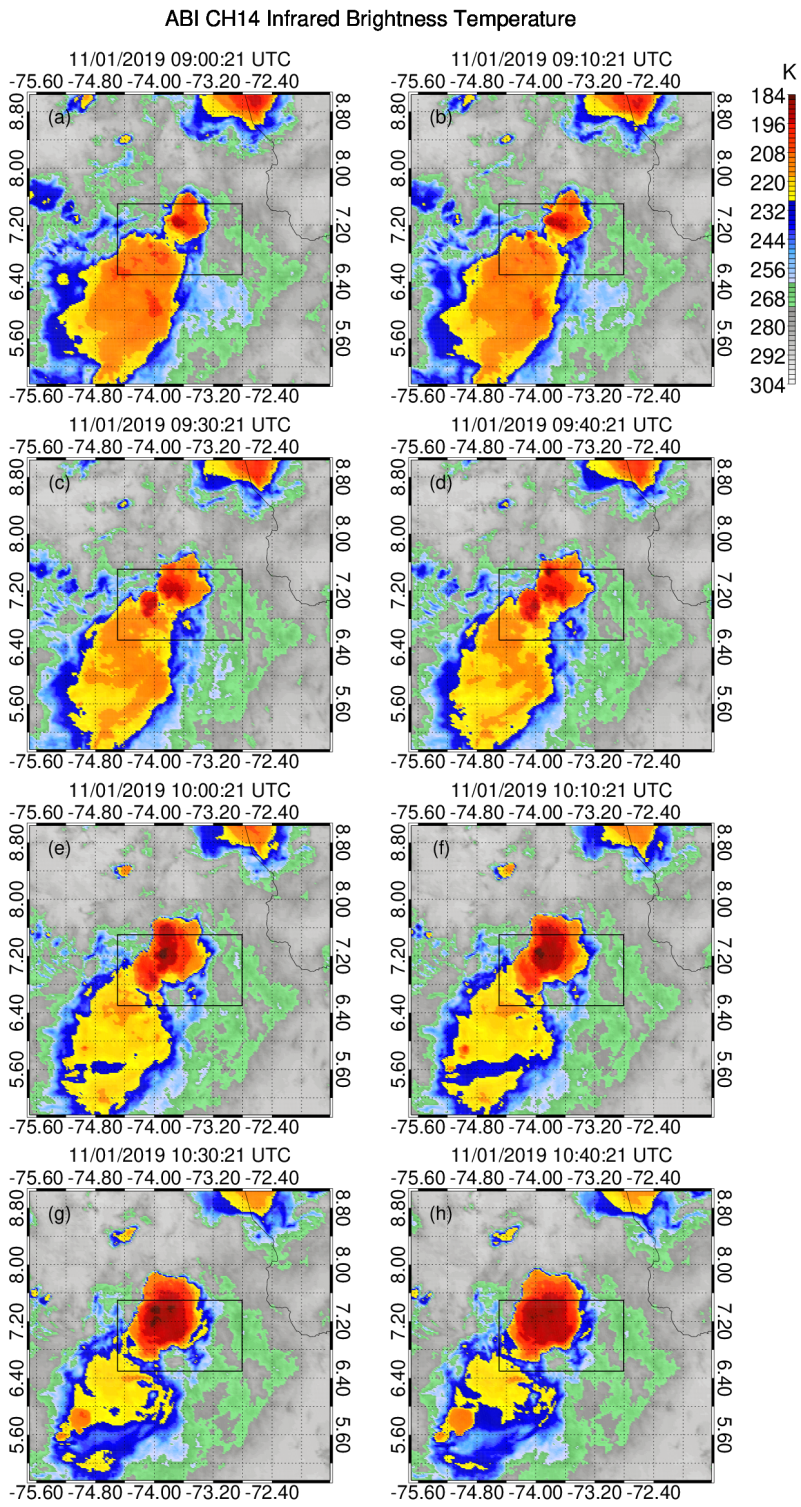

Figure 4. Maps of ABI Channel 14 (11.2 μm) infrared brightness temperature across central Colombia during the nearest ABI scans to the 15-minute GLM-CIERRA data files at (a) 09:00 UTC, (b) 09:15 UTC, (c) 09:30 UTC, (d) 09:45 UTC, (e) 10:00 UTC, (f) 10:15 UTC, (g) 10:30 UTC, and (h) 10:45 UTC. The ABI scan start times are listed in the titles for each panel. The boxes region represents the COLLMA data domain considered in this study.

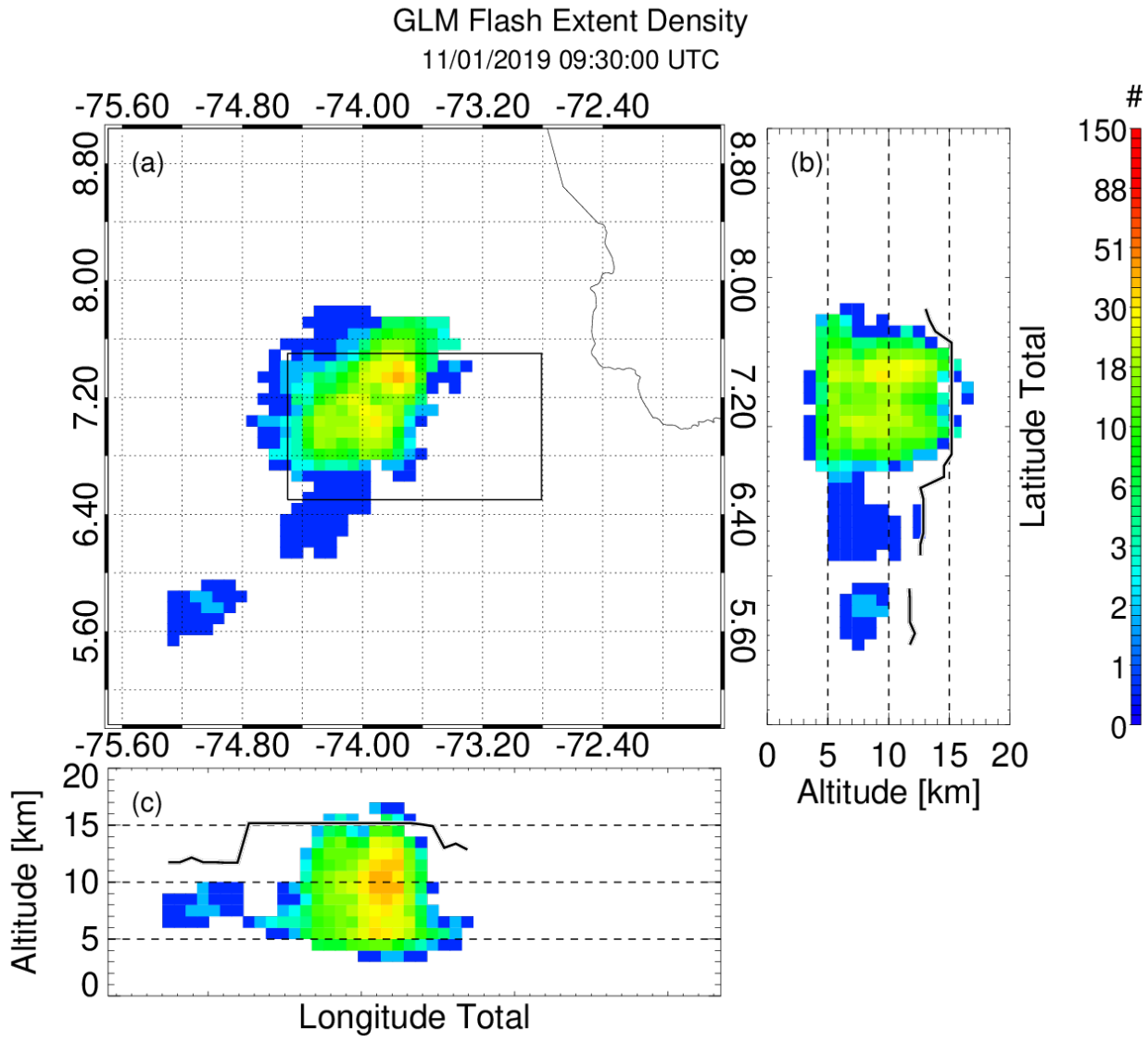

Figure 5. Volumetric FED valid from 09:30 – 09:45 UTC expressed (a) as a vertical integration, and horizontal integrations resulting in (b) a latitude-altitude distribution, and (c) a longitude-altitude distribution. The boxed region in (a) represents the COLLMA data domain, while the solid lines in (b) and (c) show the maximum ABI CTH coincident with GLM groups at each latitude or longitude.

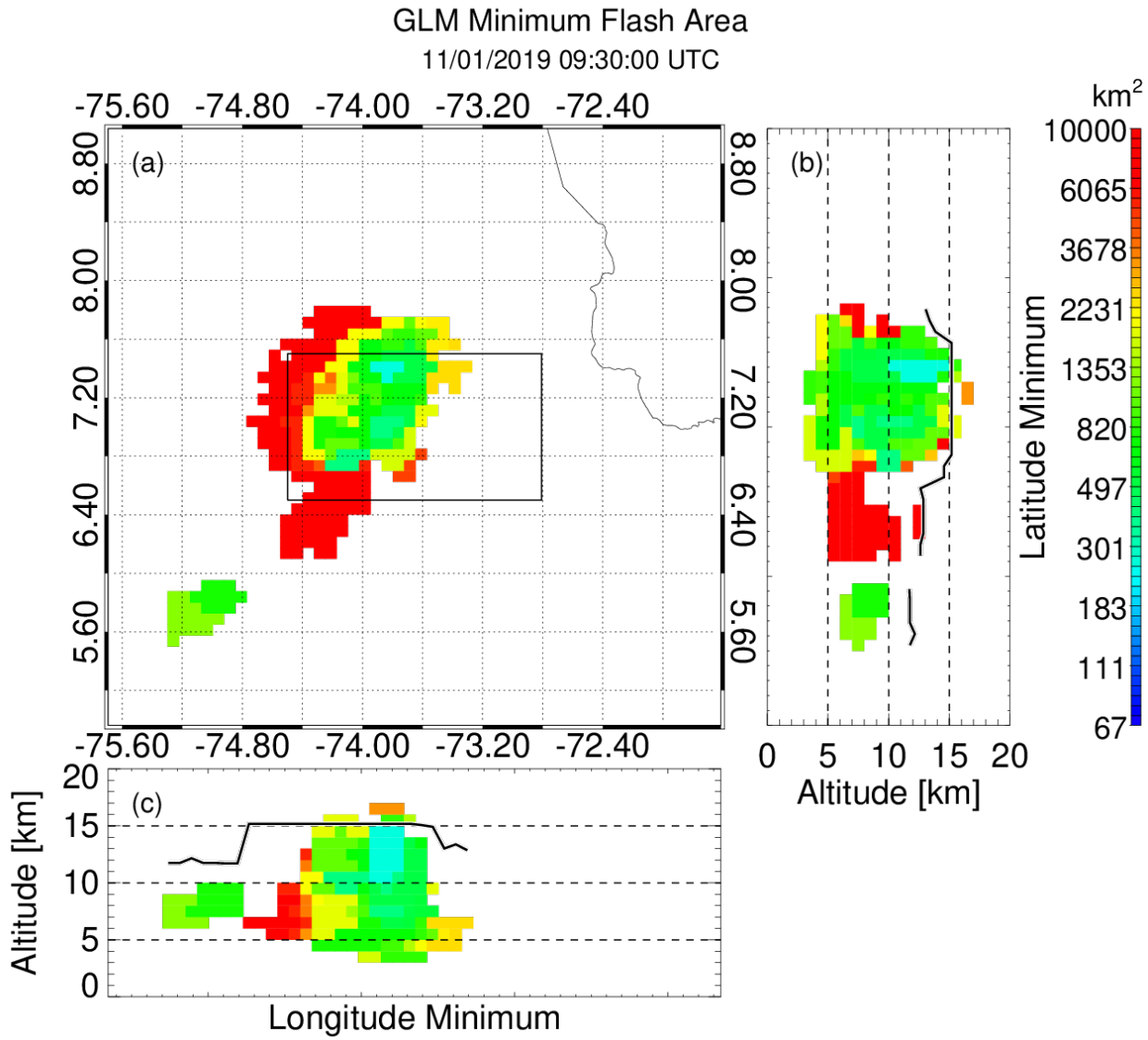

Figure 6. Volumetric MFA valid from 09:30 – 09:45 UTC, plotted as in Figure 5.

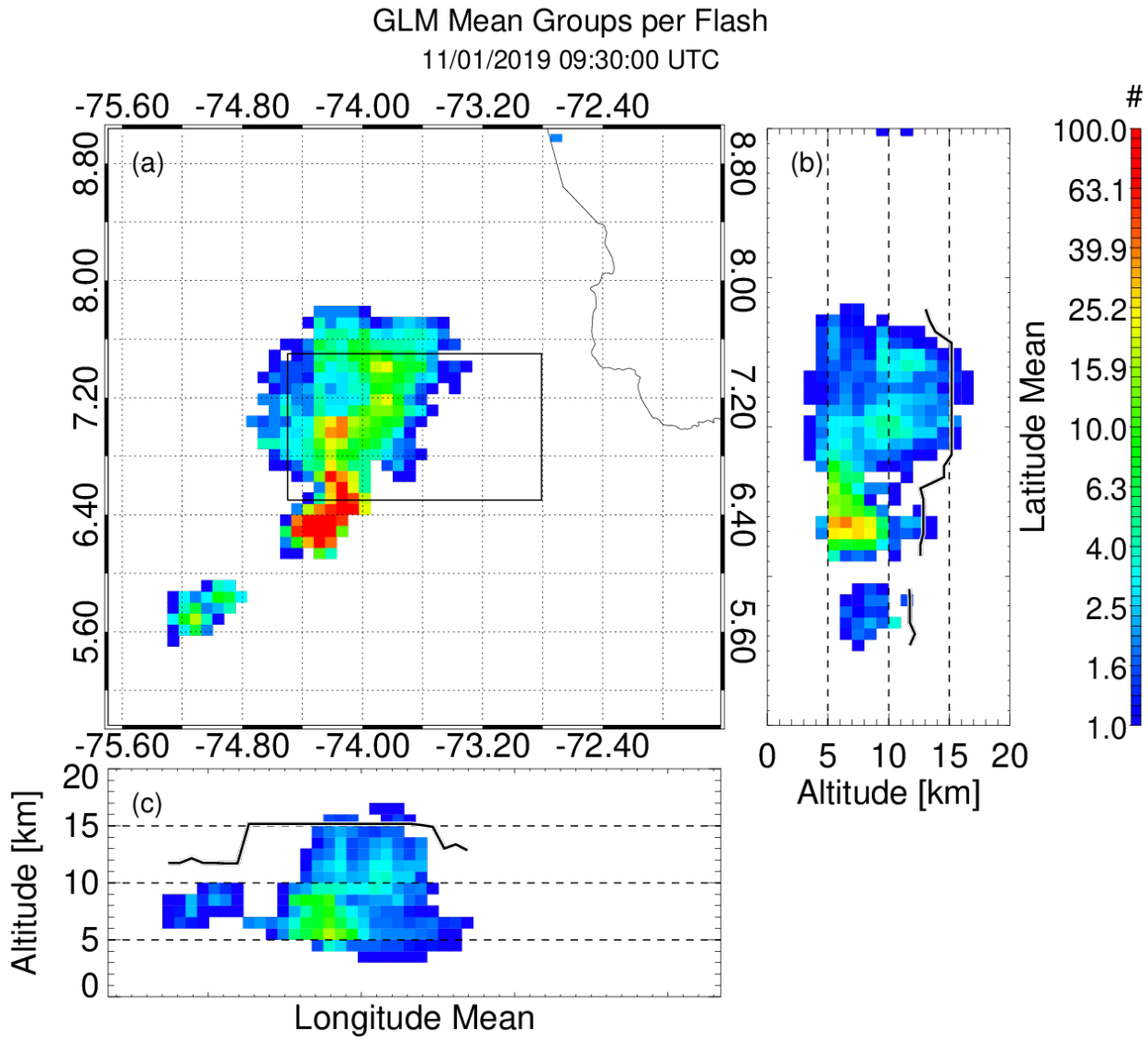

Figure 7. Volumetric GPF valid from 09:30 – 09:45 UTC, plotted as in Figure 5.

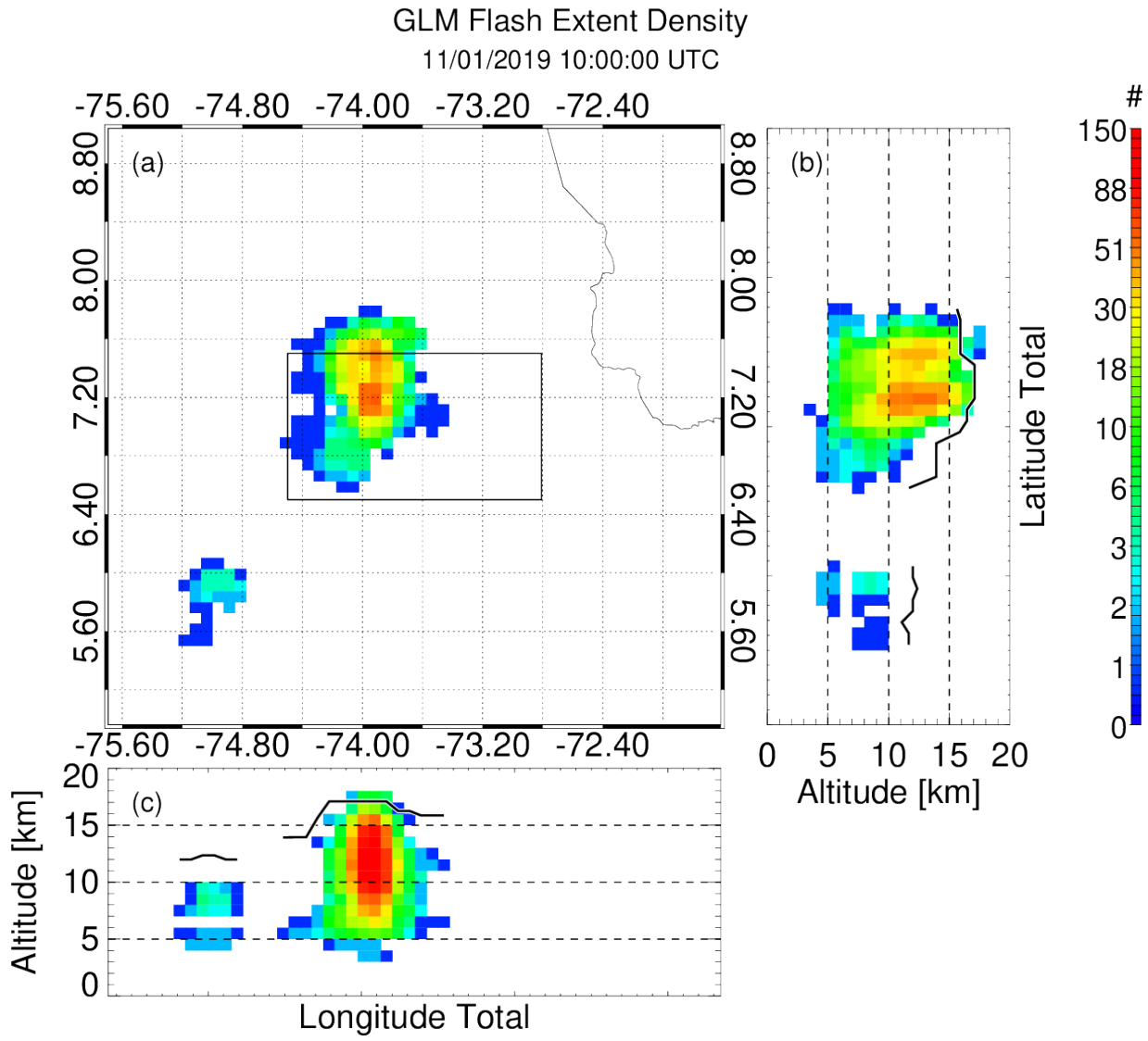

Figure 8. Volumetric FED valid from 09:45 – 10:00 UTC, plotted as in Figure 5.

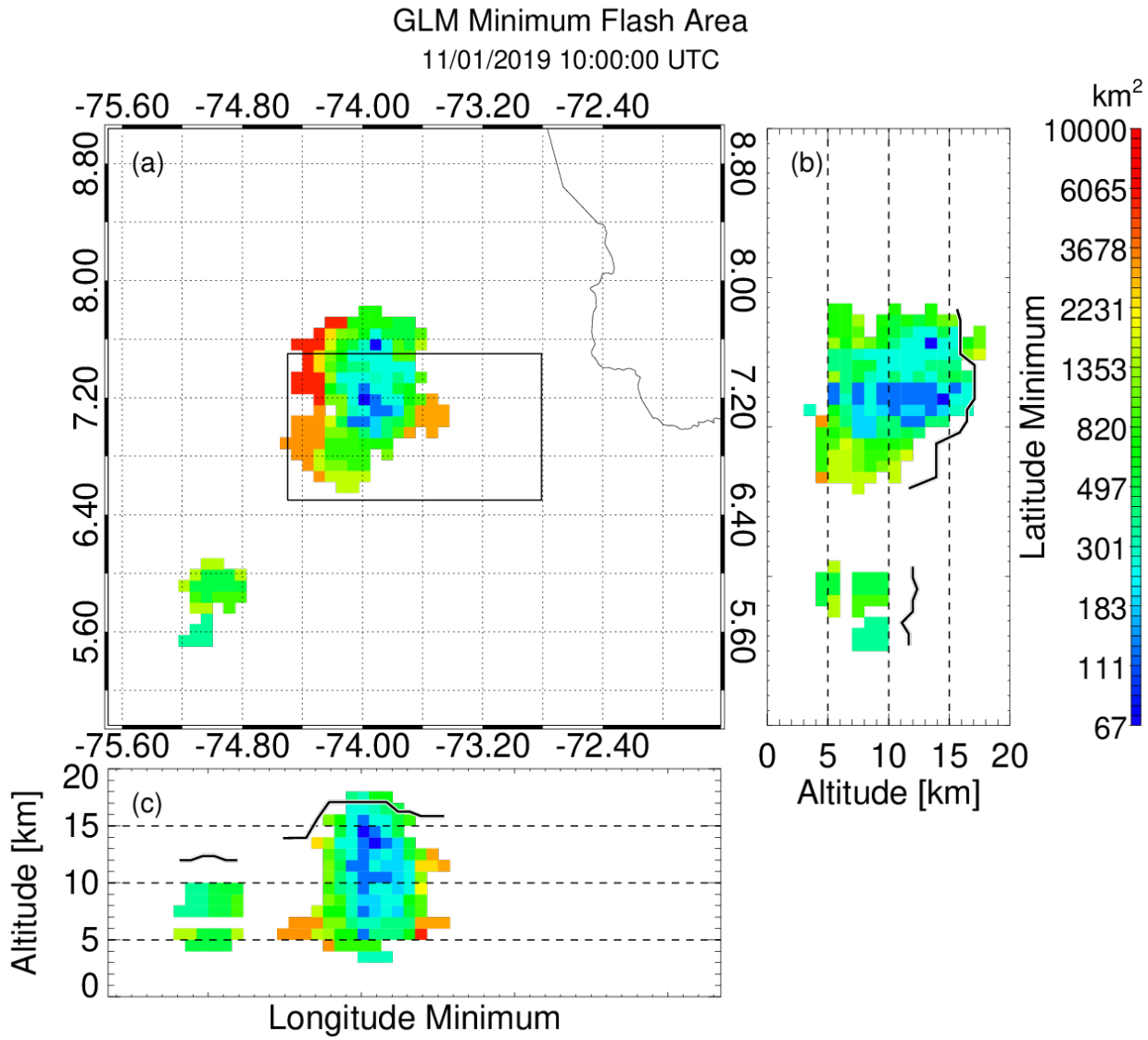

826
827
828 **Figure 9.** Volumetric MFA valid from 09:45 – 10:00 UTC, plotted as in Figure 5.

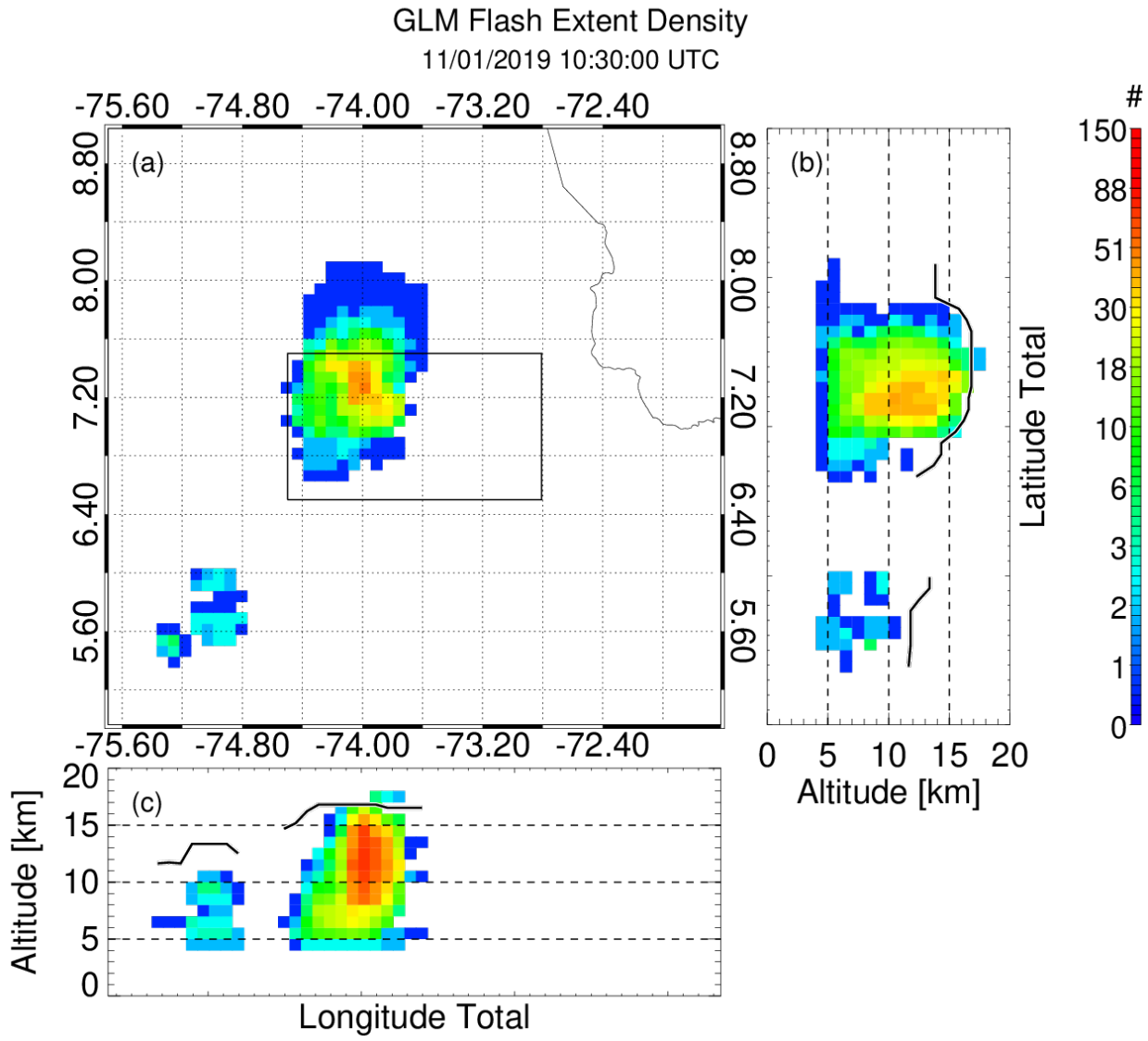

Figure 10. Volumetric FED valid from 10:30 – 10:45 UTC, plotted as in Figure 5.

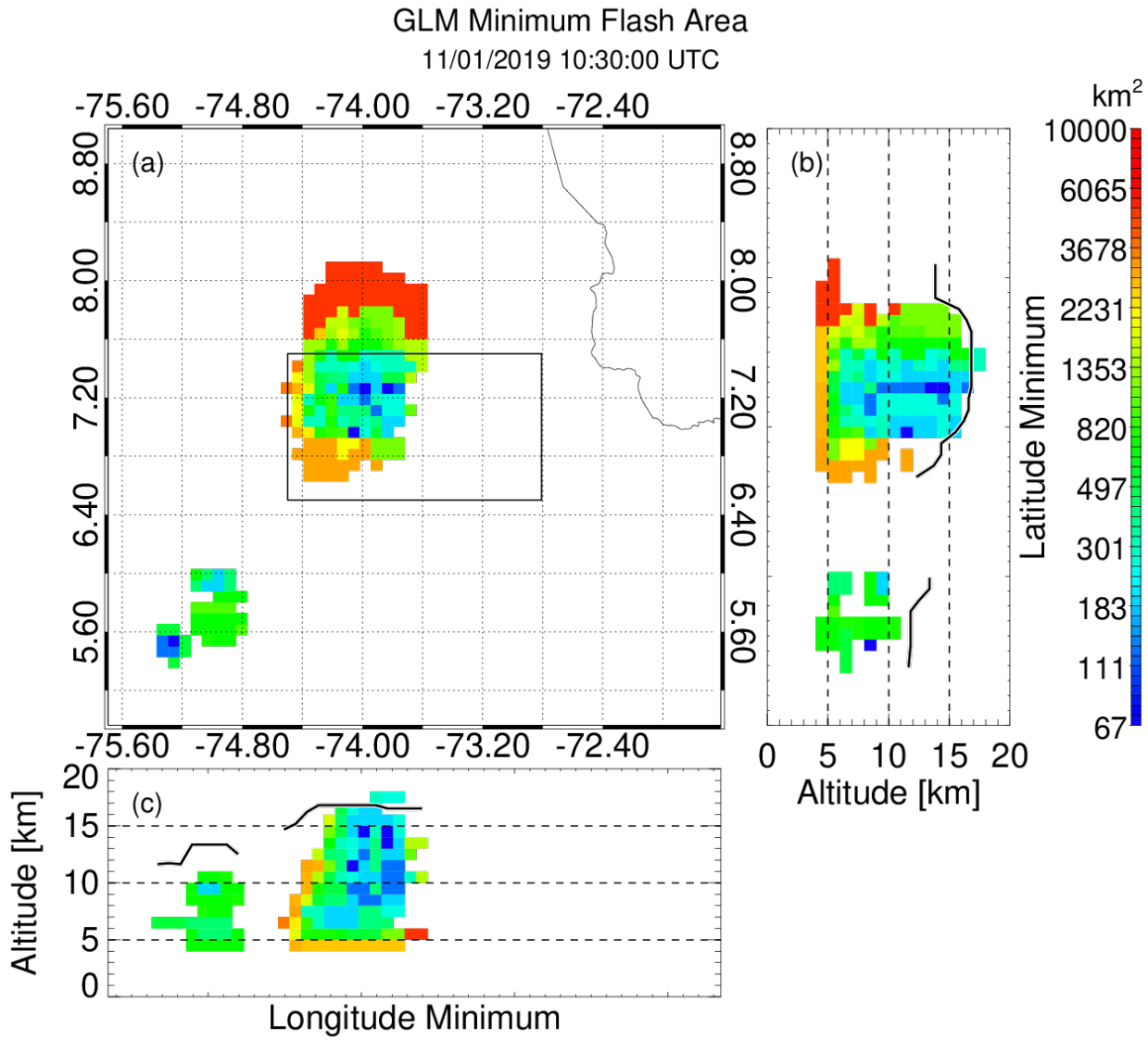

Figure 11. Volumetric MFA valid from 10:30 – 10:45 UTC, plotted as in Figure 5.

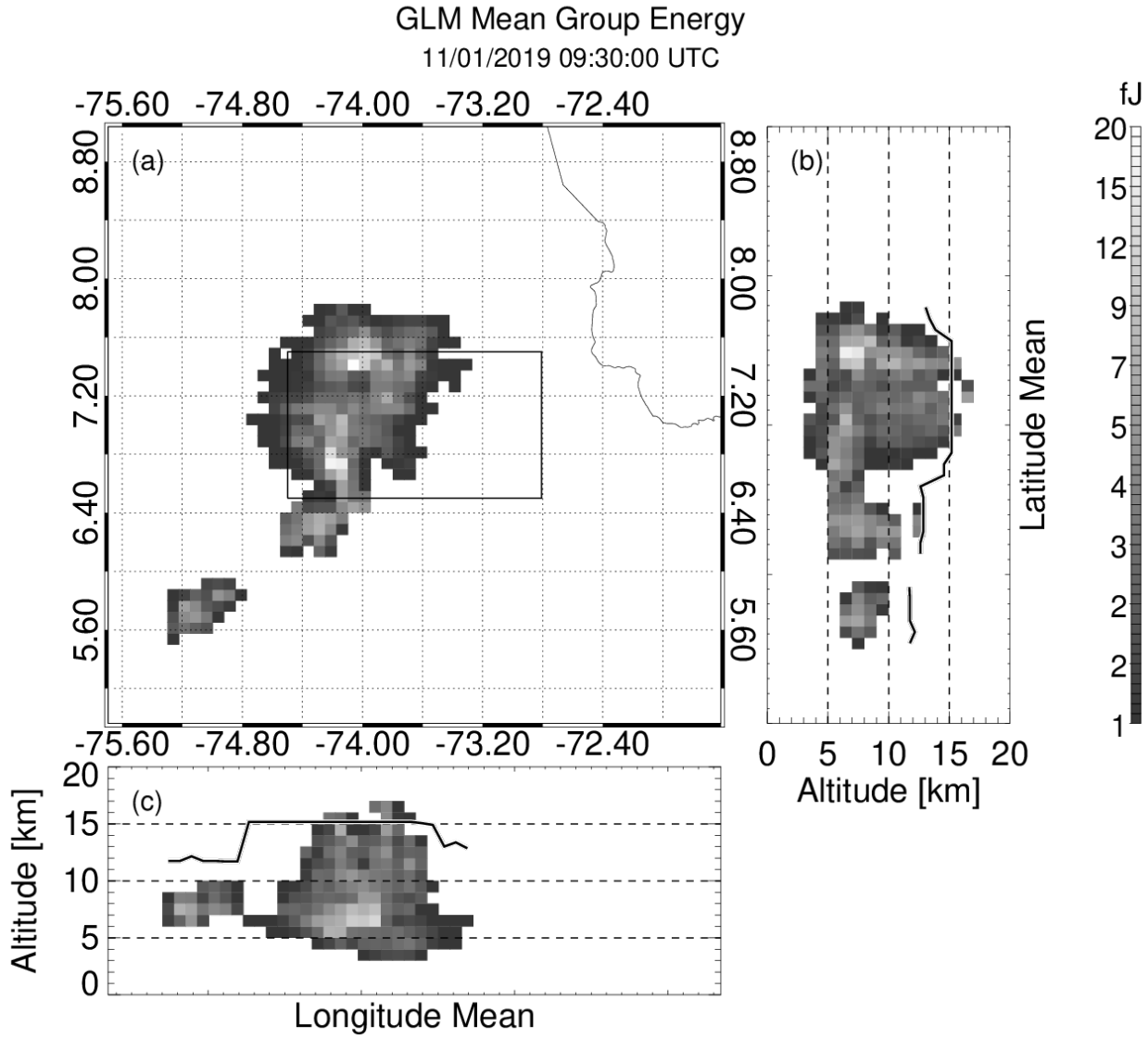

Figure 12. Volumetric MGE valid from 09:30 – 09:45 UTC, plotted as in Figure 5.

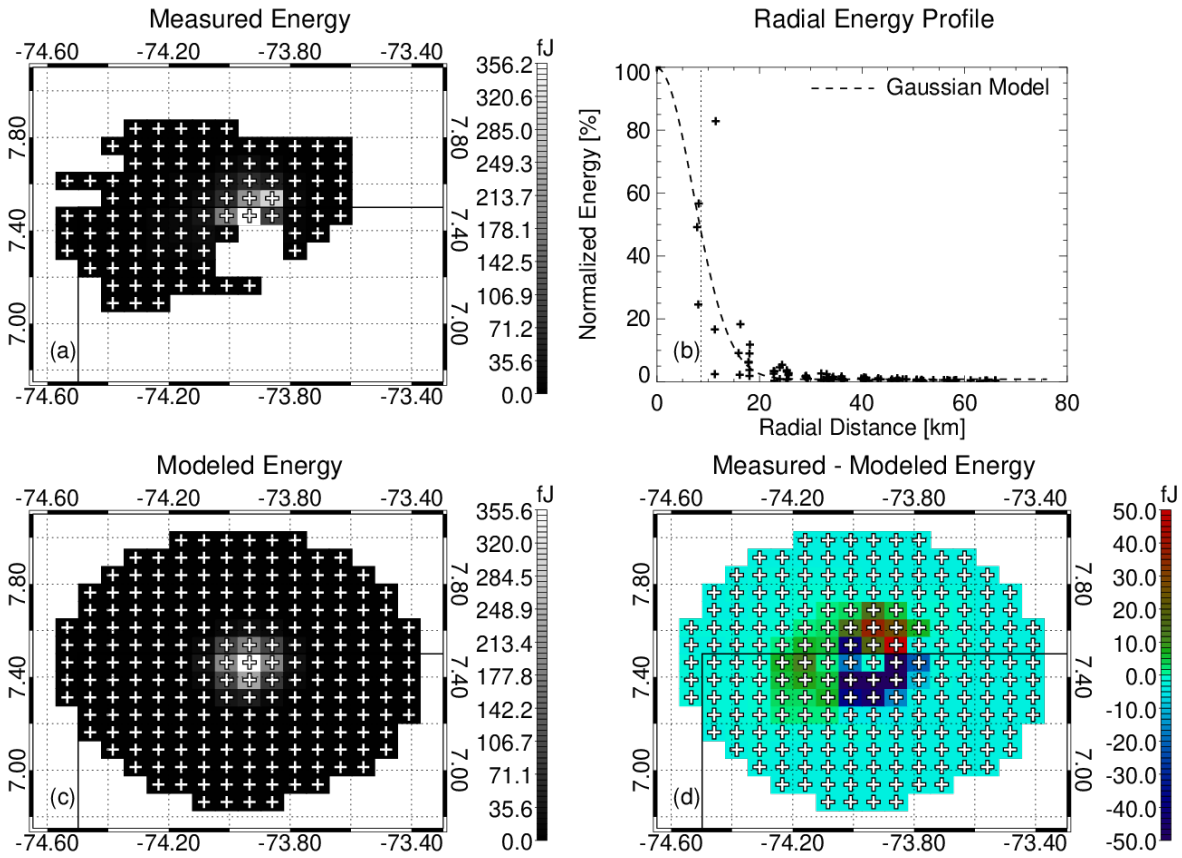

Figure 13. Spatial energy analysis for an example large GLM group located along the northern flank of the thunderstorm core. (a) Measured event energy across the group. (b) Radial energy profile relative to the brightest event in the group (plus symbols) and Gaussian model fit (dashed). The Half Width of Half Maximum (HWHM) distance is indicated with a vertical dotted line. (c) Idealized spatial energy distribution from the Gaussian model. (d) Energy difference between the GLM measurements and the Gaussian model.

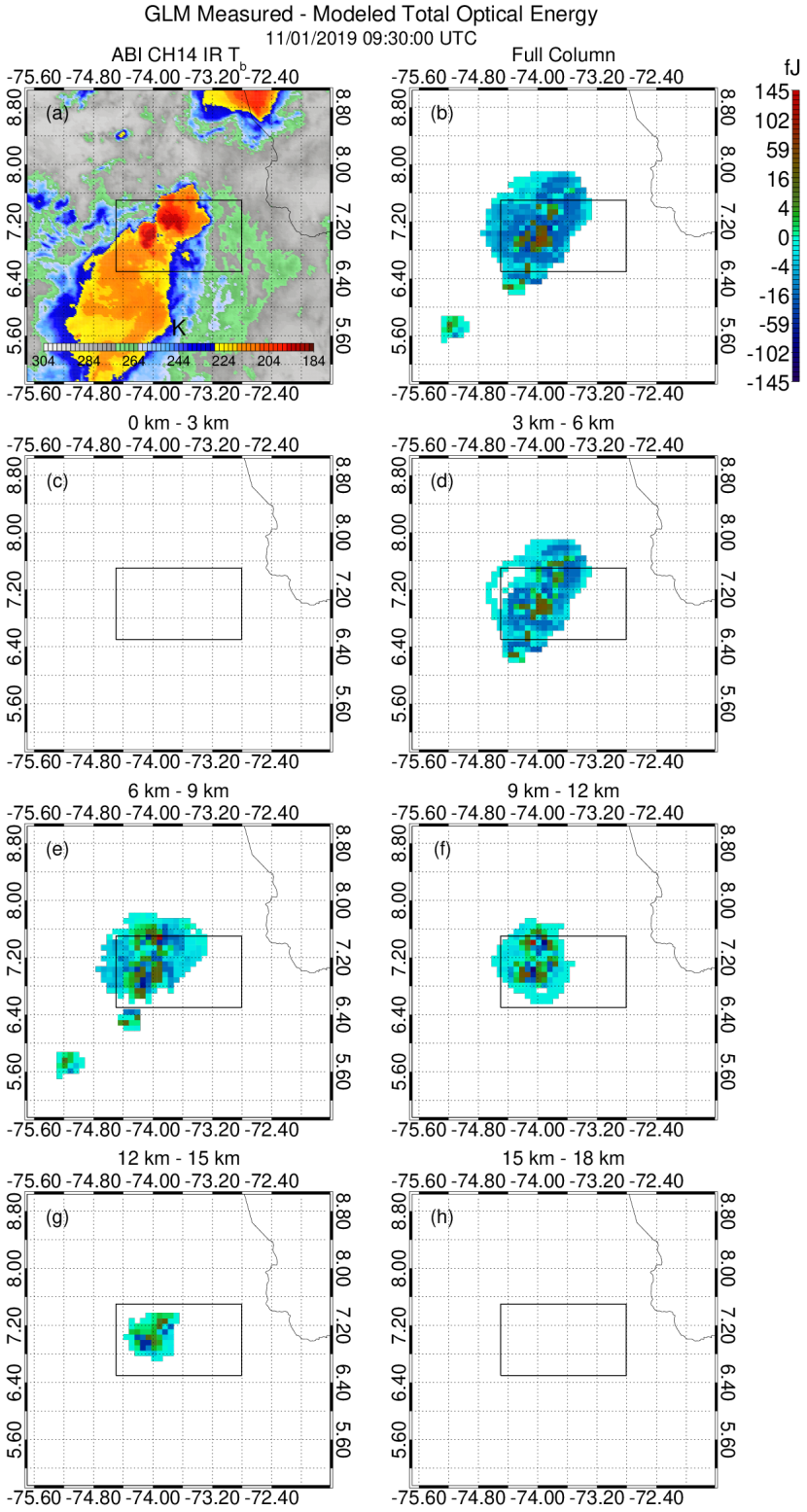

Figure 14. Maps of (a) ABI Channel 14 (11.2 μm) infrared brightness temperature and the GLM MME product as (b) a vertical integration through the full column and in layers between (c) 0-3 km, (d) 3-6 km, (e) 6-9 km, (f) 9-12 km, (g) 12-15 km, and (h) 15-18 km altitude valid at 09:30 UTC. Layers are greater than or equal to the lower limit and less than the upper limit.

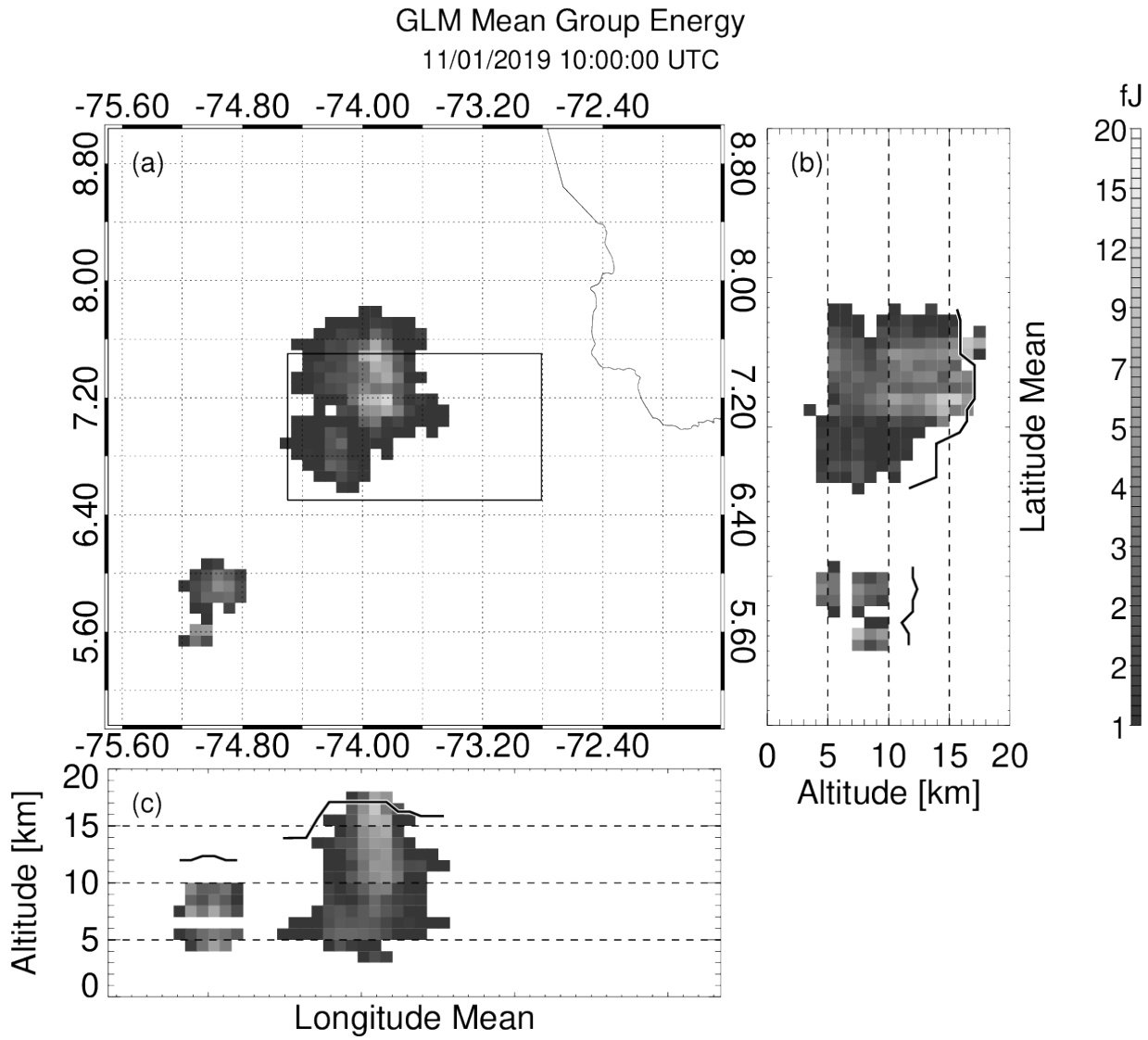

852
853 **Figure 15.** Volumetric MGE valid from 10:00 – 10:15 UTC, plotted as in Figure 5.

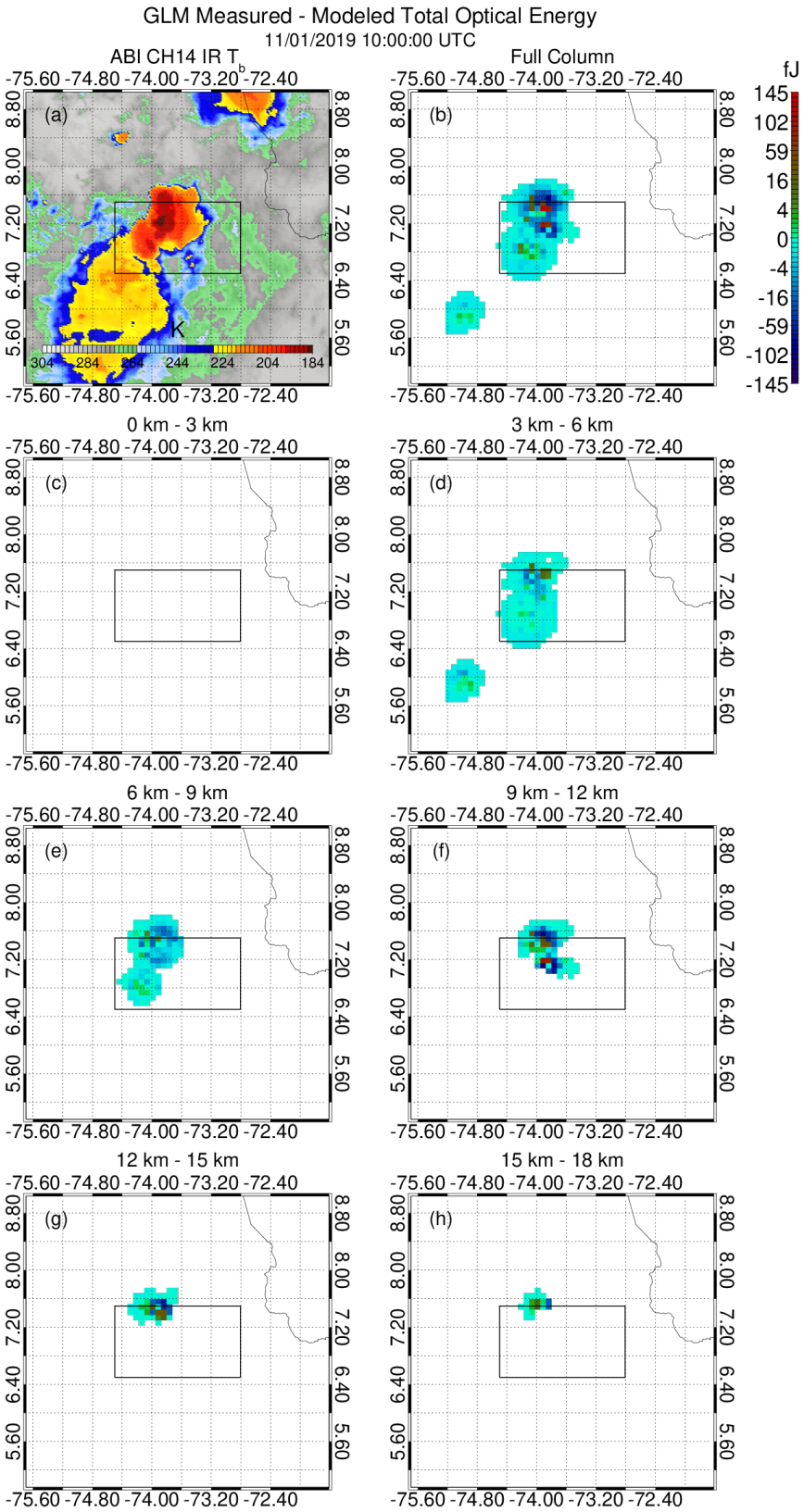

Figure 16. As in Figure 14, but valid at 10:00 UTC.